



CHORUS

This is the accepted manuscript made available via CHORUS. The article has been published as:

Monitored quantum dynamics and the Kitaev spin liquid

Ali Lavasani, Zhu-Xi Luo, and Sagar Vijay

Phys. Rev. B **108**, 115135 — Published 15 September 2023

DOI: [10.1103/PhysRevB.108.115135](https://doi.org/10.1103/PhysRevB.108.115135)

Monitored Quantum Dynamics and the Kitaev Spin Liquid

Ali Lavasani,^{1,2} Zhu-Xi Luo,³ and Sagar Vijay⁴

¹*Joint Quantum Institute, NIST/University of Maryland, College Park, MD 20742, USA*

²*Condensed Matter Theory Center, University of Maryland, College Park, MD 20742, USA*

³*Kavli Institute for Theoretical Physics, University of California, Santa Barbara, CA 93106, USA*

⁴*Department of Physics, University of California, Santa Barbara, CA 93106, USA*

Quantum circuit dynamics with local projective measurements can realize a rich spectrum of entangled states of quantum matter. Motivated by the physics of the Kitaev quantum spin liquid [27], we study quantum circuit dynamics in (2+1)-dimensions involving local projective measurements, in which the monitored trajectories realize (i) a phase with topological quantum order or (ii) a “critical” phase with a logarithmic violation of area-law-scaling of the entanglement entropy along with long range tripartite entanglement. A Majorana parton description of these dynamics, which provides an out-of-equilibrium generalization of the parton description of the Kitaev honeycomb model, permits an analytic understanding of the universal properties of these two phases, including the entanglement properties of the steady-state, the dynamics of the system on the approach to equilibrium, and the phase transition between these states. In the topologically-ordered phase, two logical qubits can be encoded in an initial state and protected for a time which scales exponentially in the linear dimension of the system, while no robust encoding of quantum information persists in the critical phase. Extensive numerical simulations of these monitored dynamics confirm our analytic predictions.

I. INTRODUCTION

Quantum spin liquids [2, 3, 54] and topological orders characterized by long-range entanglement [63] have advanced our understanding of the possible phases of quantum matter. In equilibrium, quantum spin liquids can arise from frustration; examples include geometric frustration in non-bipartite lattices such as the nearest-neighbor Heisenberg model on the Kagomé lattice [10, 11, 23, 25, 35, 41, 52, 57, 61, 64], competition between longer-ranged and shorter-ranged interactions such as the nearest and second-nearest neighbor Heisenberg model on the triangular lattice [21, 24, 26, 69], and anisotropic interactions such as the celebrated Kitaev honeycomb model [27].

The search for material realizations of quantum spin liquids remains challenging due to the requirement of strong correlations, while definitive signatures of spin liquids can be difficult to experimentally probe. On the other hand, digital quantum simulators [1] have recently emerged as a platform for using controllable operations to simulate interesting phases of quantum condensed matter. Therefore, it is natural to consider constructive way to design long-range entangled states in this setting using local unitary operations and projective measurements.

In this work, we exploit non-commutative, projective measurements as a new source of frustration to generate out-of-equilibrium analogues of spin liquid states. Specifically, we consider projective measurements of the competing anisotropic interactions in the Kitaev honeycomb model [27]. When these measurements are performed in a spatially random fashion, we find that the monitored trajectories of the quantum many-body system produce analogues of the two phases in the original Kitaev model, as the relative rate of the different kinds of measurements are tuned: (i) a topologically-ordered phase with

long-range entanglement, and area-law scaling of the entanglement entropy and (ii) a “critical” phase with a logarithmic violation of area-law entanglement and long-range tripartite entanglement. The latter phase appears to resemble a state in which the Majorana partons of the Kitaev spin liquid have formed a Fermi surface, which cannot occur in the ground-state of the Kitaev spin liquid on the honeycomb lattice while preserving time-reversal and translation symmetry [27]. Through analytical arguments and numerical studies, we argue that these two phases are robust in the presence of other perturbations, such a small rate of additional projective measurements.

An analytic understanding of these phases is obtained by invoking a Majorana-fermion parton representation, which has been previously used to re-cast the honeycomb model as a model of Majorana fermions coupled to a static \mathbb{Z}_2 gauge field [27]. The dynamics that we consider can be formulated as the dynamics of the Majorana partons evolving under the action of local measurements, followed by a projection back into the physical spin Hilbert space. A limit of these measurement-only dynamics admits a particularly simple representation in terms of the Majorana partons, allowing for an understanding of the universal properties of the topologically-ordered and critical phases, as well as the phase transition between them. This representation is also used to argue in general terms that certain high-symmetry regimes of these measurement-only dynamics must give rise to either a topologically-ordered phase for the monitored pure-states or a phase in which these states have super-area-law scaling of the entanglement entropy. We note that the far-from-equilibrium parton construction invoked in this work could potentially be useful to study other long-range-entangled phases of quantum matter that can emerge in monitored quantum dynamics.

We note that quantum circuits with both projective

measurements and local unitary gates (“hybrid” circuits) have been extensively studied to uncover a rich behavior of the monitored pure-state trajectories. In (1+1)-dimensions, these dynamics can give rise to a new phase of volume-law-entangled quantum matter [39] with close connections to the theory of quantum error-correcting codes [9, 12, 14, 38, 66]. Dynamics in which the measurements and unitary gates commute preserve a global symmetry can give rise to monitored trajectories that exhibit symmetry-protected topological order [33] and spin-glass order [53]. In (2+1)-dimensions, hybrid quantum circuits can yield monitored pure-states with truly long-range entanglement [34]. Previous studies on the emergence of topological order in measurement-only circuits have considered the competition between different sets of measurements, where each set is composed of mutually commuting operators that stabilizes a certain phase. For instance, Ref.[34] studied the competition between measurements of the toric code stabilizers, which stabilizes the toric code phase, and single qubit measurements, which stabilizes a trivial phase. In contrast, for the circuit model which is studied in this work, subsets of mutually commuting operators do not stabilize any interesting phase, and non-commuting measurements are crucial for the emergence of the non-trivial phases. Moreover, the lower weight of the measurements used in the circuit could make experimental investigation of the phase diagram more feasible.

The remainder of the paper is organized as follows. A detailed summary of the key results is presented in Sec. IA. In Section II we introduce the circuit model considered in this work and we provide a general analytical understanding of the corresponding entanglement dynamics using the Majorana parton description of the steady-state of the circuit. In particular, Section IIA present the Majorana parton representation of the dynamics of the monitored pure-states, Section IIB uses the parton representation to obtain general analytical results regarding the entanglement structure and topological order of the quantum trajectories and Section IIC explains how one can describe the dynamics of the Majorana partons in terms of a classical fully pack loop model in three dimensions and use that to argue about possible entanglement phases in this system. In Section III we discuss analytically the purification dynamics of the circuit model in each phase. The numerical results are presented in Section IV which supports the analytical arguments that are presented in previous sections. In Section V we study small perturbations to the monitored dynamics studied in Sec. II, and show through a combination of numerical and analytic arguments that the critical and topologically-ordered phases remain stable. We conclude with a short discussion and outlook in Section VI.

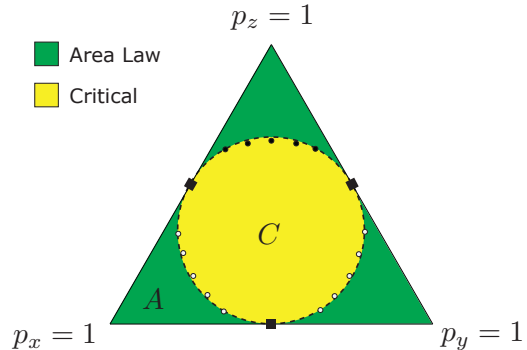


FIG. 1: **Phase diagram:** As the probabilities of measuring different bond operators (p_x, p_y, p_z with $p_x + p_y + p_z = 1$) are tuned, the monitored pure-state trajectories realize (i) a topologically-ordered phase with an area-law scaling of the entanglement entropy (green regions) or (ii) a “critical” phase with a logarithmic violation of area-law entanglement scaling along with long-range tripartite entanglement (yellow regions). The black dots show the numerically-extracted phase transition from simulations of these dynamics, while the remaining dots are obtained by $\pi/3$ rotations. The topologically-ordered and critical phases are robust when the dynamics are perturbed, e.g by adding a small rate of single-qubit projective measurements.

A. Summary of Results

The monitored random circuit studied here is inspired by the Kitaev honeycomb model [27]. We consider the same arrangement of qubits on an $L \times L$ honeycomb lattice with periodic boundary conditions. We first study dynamics involving projective measurements of the nearest-neighbor interaction terms in the Kitaev honeycomb model [27], which depend on the orientation $j \in \{x, y, z\}$ of the bond connecting the two qubits: at each updating step of the circuit, a random two-qubit operator along a bond of type j is measured with probability p_j (with $p_x + p_y + p_z = 1$); these operators and the arrangement of qubits are discussed in greater detail in Sec. II. A time step is defined to be N consecutive updating steps. As these measurement rates are tuned, the monitored pure-state trajectories of the system support two distinct phases, as summarized in Fig. 1:

- (i) *Topologically-Ordered Phase:* For highly biased measurement probabilities (e.g. $p_z \gg p_x, p_y$) corresponding to the green regions in Fig. 1, the monitored pure-states exhibit topological order. In addition to exhibiting area-law scaling of the von Neumann entanglement entropy¹, the steady-state of

¹ We use the following definition of the von Neumann entropy of

the monitored dynamics exhibits long-range entanglement, as evidenced by a quantized topological entanglement entropy [28, 36] $S_{\text{topo}} = 1$ as well as a bipartite mutual information between two non-contractible regions on the torus and separated by $O(L)$ distance, which is equal to 1.

The evolution of a maximally-mixed initial state in this dynamical regime further reveals the persistent, long-ranged entanglement in this phase. Projective measurements have the effect of rapidly disentangling the maximally-mixed initial state, resulting in an exponential decay of the entanglement entropy until it plateaus at 2. This plateau persists until a time $t_{\text{purif}} \sim O(\exp(L))$, when the system completely purifies. This protected information which survives until exponentially long times in the system size corresponds to the entanglement between the environment and two operators which loop around the topologically non-trivial cycles of the torus, and suggests the emergence of a dynamically generated quantum code with two logical qubits.

In contrast, we note that the Kitaev honeycomb model does not encode any logical qubits as a subsystem code [59], while the recently-discovered honeycomb code [20] uses a time-periodic schedule of measurements to protect two logical qubits. In contrast, the topologically-ordered phase that we find demonstrates that randomness in measurement order can also lead to the emergence of a long-lived logical subspace.

- (ii) *Critical Phase:* A “critical” phase is found in region C in Fig. 1. In this phase, the entanglement entropy of a large subsystem A scales with its linear dimension L_A as

$$S_A = c_0 L_A \log L_A + \dots \quad (1)$$

where the ellipsis denotes sub-leading corrections, and c_0 is a non-universal constant. Furthermore, on the torus, the bipartite mutual information between two non-contractible regions of width $O(L)$ separated by a similar distance, denoted $I_2(L)$, scales linearly with L . The critical phase also supports multi-partite long range entanglement as quantified by the negative tripartite mutual information between non-contractible regions, in contrast to the area-law phase. Finally, the magnitude of the expectation value of open Wilson lines with endpoints separated by a distance r decays as a power law $1/r^\Delta$ with $\Delta = 3$.

The purification dynamics in the critical phase is quite different from the area law phase. Starting

from a totally mixed state, there is an initial exponential drop, followed by $1/t$ decay of entanglement entropy of the system, which can be understood as a “Lévy flight” annihilation process of unpaired Majorana partons. The system completely purifies at a time $t_{\text{purif}} \sim O(L^2)$. No logical information is protected in this phase.

We also consider small perturbations to these dynamics, e.g. single-qubit or other multi-site measurements, which have the important effect of removing the extensive number of conserved quantities which are present in dynamics involving only bond measurements. Through a combination of numerical and analytical arguments, we show that the critical and topologically-ordered phases persist in the presence of these perturbations.

We may compare the entanglement properties of these monitored trajectories with the phases of the Kitaev spin liquid. In the presence of time-reversal and translational symmetry, the Kitaev spin liquid on the honeycomb lattice [27] has two phases: a gapless phase where the Majorana partons have a semi-metallic dispersion, and three gapped phases which each exhibit \mathbb{Z}_2 topological order, and are related to each other by three-fold ($\theta = 2\pi/3$) spatial rotations. The area-law-entangled phase that arises in the monitored dynamics that we study is quantitatively similar to the \mathbb{Z}_2 topological order that arises in the ground-state of the Kitaev honeycomb model, due to the quantized topological entanglement entropy, and the ability to encode two logical qubits on the torus. As discussed in Sec. II A, the quantized bipartite mutual information between a pair of non-contractible regions on the torus is also shared by a particular ground-state sector of the two-dimensional \mathbb{Z}_2 toric code on the torus, into which we argue that the steady-state of the measurement-only dynamics purifies when the measurement rates are highly anisotropic.

In contrast to these area-law-entangled phases [65], the critical phase quantitatively resembles a state in which the Majorana partons in the Kitaev spin liquid have formed a Fermi surface, due to both (i) the scaling of the entanglement entropy with subsystem size and (ii) the extensive scaling of the bipartite mutual information $I_2(L) \sim L$. Such a state cannot emerge in the ground-state of the Kitaev spin liquid in the presence of time-reversal and translation symmetry. Since the critical phase of the monitored dynamics arises when measurements are applied randomly in space, translation symmetry is not present in any typical realization of the dynamics, though it is preserved by the statistical ensemble of monitored pure-states. As a result, a more appropriate comparison may be to the Kitaev honeycomb model with broken translation symmetry, e.g. by introducing randomness in the spin exchange interaction [29], which can produce an effective description of the Majorana partons with random hopping matrix elements on a bipartite lattice, which could lead to a “metallic” phase for the partons [43] in which states at zero-energy are delocalized. The entanglement properties of such a phase are

a density matrix ρ throughout this work as $S(\rho) = -\text{Tr}[\rho \log_2 \rho]$

not known to us, however, and we are unable to draw any further quantitative comparisons between this phase and the critical phase of the monitored dynamics.

Finally, perturbations which break time-reversal symmetry, such as an external magnetic field, can drive the gapless phase of the Kitaev honeycomb model into a gapped, chiral spin liquid supporting non-Abelian anyons [27]. Furthermore, in the presence of both strong disorder and broken time-reversal symmetry, the Majorana partons can form a metallic state [31] in which the fermionic parton wavefunctions $\psi_n(\mathbf{r})$ are spatially-extended [6, 55], as quantified by a non-trivial scaling of the inverse participation ratios (IPR) with system size L as $I_q = \int d^2r |\psi_n(\mathbf{r})|^{2q} \sim L^{-(q-1)D_q}$, with D_q a q -dependent constant. Analogous perturbations to the measurement-only dynamics that we consider, such as single-qubit projective measurements, do not appear to qualitatively alter the entanglement properties of the critical phase. Furthermore, the stabilizer nature of the dynamics that we study, as clarified in Sec. II, necessarily prevents the parton wavefunctions from being spatially extended in a manner which is characteristic of this disordered, metallic phase.

We also study phase transitions between the critical and topologically-ordered phases in this monitored dynamics. We argue that the generic nature of the phase transition is related to a geometrical phase transition in a three-dimensional classical loop model, which has arisen in a different context in the study of measurement-only dynamics of free fermions [48]. The tripartite mutual information, which serves as an order parameter for the phase transition between the critical and topologically-ordered phases, is used to numerically extract the correlation length critical exponent $\nu \approx 0.9$ consistently at distinct phase transition points in the bulk of the phase diagram. This value is close to the numerically-obtained value of this exponent from previous studies of this phase transition [49, 56]. We note that the transitions at the boundary of the phase diagram, e.g. $p_z = 0$, can be understood by mapping the growth of local operators which stabilize the evolving wavefunction to the problem of bond percolation in two spatial dimensions, which is in a different universality class from the phase transition between the critical and topologically-ordered phases.

II. MONITORED DYNAMICS

We now describe the monitored dynamics in detail. Consider a system of $N = 2L^2$ qubits arranged on vertices of a $L \times L$ honeycomb lattice with periodic boundary condition. On each edge of the honeycomb lattice connecting sites \mathbf{r} and \mathbf{r}' , we define a *bond operator* depending on the orientation of the edge and which acts on the two qubits as $X_{\mathbf{r}}X_{\mathbf{r}'}$, $Y_{\mathbf{r}}Y_{\mathbf{r}'}$ or $Z_{\mathbf{r}}Z_{\mathbf{r}'}$ (see Fig.2). Starting from a maximally-mixed initial state $\rho = \mathbb{1}/2^N$, we choose a bond of type x , y , or z randomly with probability p_x , p_y or p_z respectively ($p_x + p_y + p_z = 1$),

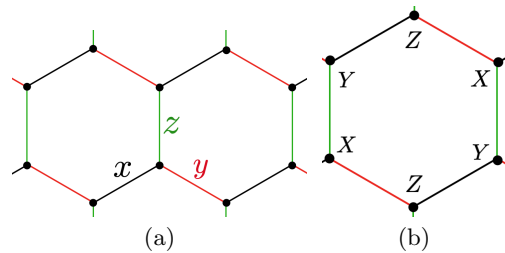


FIG. 2: **Dynamics:** Qubits degrees of freedom reside on the sites of the honeycomb lattice. Bonds of the lattice are of type $j \in \{x, y, z\}$ shown in (a) and a bond operator is defined as the product of the two Pauli operators of type j along that bond. A plaquette operator W_p is defined as the product of bond operators over an elementary plaquette, as shown in (b).

and we measure the corresponding two-qubit bond operator, with measurement outcomes obtained according to Born's rule. A time step of these dynamics corresponds to N consecutive measurements.

We note that product of bond operators around an elementary plaquette p of the honeycomb lattice, as shown in Fig. 2b, commutes with all of the bond operators; we refer to this as the *plaquette operator* W_p . As a result, a monitored dynamics involving measurements of bond operators contains extensively many conserved quantities. In Sec. V, we will consider perturbing away from these dynamics in such a way that this conservation law is no longer microscopically maintained.

A. Parton Description of the Steady-State

We now explore the steady-state entanglement properties of the monitored pure-state of the system as a function of the probabilities p_x , p_y , p_z . To make analytic progress, we replace each qubit with four Majorana fermions with fixed fermion parity so that the Pauli spin operators at lattice site \mathbf{r} are represented as $X_{\mathbf{r}} = ib_{\mathbf{r}}^x c_{\mathbf{r}}$, $Y_{\mathbf{r}} = ib_{\mathbf{r}}^y c_{\mathbf{r}}$, and $Z_{\mathbf{r}} = ib_{\mathbf{r}}^z c_{\mathbf{r}}$ [27]. It is convenient to arrange the fermions within each lattice site so that each b^j Majorana fermion lies at the end of a bond of type j . By requiring that the fermion parity is constrained at each site as $b_{\mathbf{r}}^x b_{\mathbf{r}}^y b_{\mathbf{r}}^z c_{\mathbf{r}} = -iX_{\mathbf{r}}Y_{\mathbf{r}}Z_{\mathbf{r}} = 1$, we faithfully recover the spin Hilbert space.

The monitored pure state of the spins evolves through the application of local projectors, which correspond to a sequence of local measurements and outcomes, which are drawn according to Born's rule. Within a particular monitored trajectory, the dynamics of the spins may be re-cast as a dynamics for the Majorana partons, followed by a projection $P \equiv \prod_{\mathbf{r}} (1 + c_{\mathbf{r}} b_{\mathbf{r}}^x b_{\mathbf{r}}^y b_{\mathbf{r}}^z) / 2$ back into the Hilbert space of the spins, due to the fact that the projector P commutes with any operator acting on the spin degrees of freedom. As a concrete example, let $|\psi_f\rangle$ be a state of the Majorana partons, while $|\Psi\rangle \sim P|\psi_f\rangle$ be

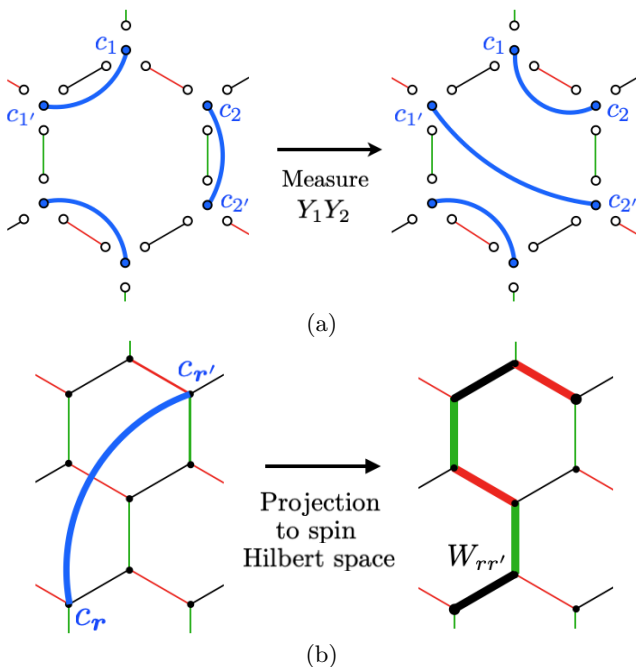


FIG. 3: **Parton Dynamics:** A projective measurement of a bond operator gives rise to a dynamics of the Majorana partons as shown in (a) and described in Sec. II A. Each pair of dimerized Majorana fermions $i c_r c_{r'} = \pm 1$ in the parton wavefunction gives rise to a stabilizer in the spin Hilbert space, which has support along a string connecting r, r' as shown in (b).

the corresponding wavefunction for the spins. A measurement of a single-qubit operator X_r which yields the outcome $+1$ modifies the state of the spins, up to normalization, as $[(1 + X_r)/2] |\Psi\rangle \sim P[(1 + i b_r^x c_r)/2] |\psi_f\rangle$. The latter expression may be interpreted as a dynamics for the Majorana parton wavefunction $|\psi_f\rangle$ followed by a projection into the spin Hilbert space.

While a monitored trajectory of the spins corresponds to a monitored evolution of the Majorana partons, we note an important difference in the probability distribution of monitored trajectories between these two kinds of dynamics. If ρ_f is the density matrix of the Majorana partons, so that $\rho = P\rho_f P / \text{Tr}(P\rho_f)$ is the corresponding state of the spins, then a measurement of a Pauli operator \mathcal{O} yields the two possible outcomes with probability $p_{\pm} = \text{Tr}(P\Pi_{\pm}\rho_f) / \text{Tr}(P\rho_f)$, respectively, where $\Pi_{\pm} = (1 \pm \mathcal{O})/2$. This is *a priori* different from the probability distribution $\text{Tr}(\Pi_{\pm}\rho_f)$ of obtaining these outcomes when measuring the corresponding operator in the state of the Majorana partons². Below, however, we will

² A simple example of such an observable is the operator $b_r^x b_r^y b_r^z c_r$; this operator is mapped to the identity within the spin Hilbert space, and thus has only one possible outcome when “measured”. In contrast, the operator $b_r^x b_r^y b_r^z c_r$ can take on various values depending on the precise state of the Majorana partons.

focus on understanding the monitored pure-state trajectories when ρ describes a stabilizer state [15], for which the entanglement properties of the evolving pure-state are sensitive to the Pauli operators which are measured, but insensitive to their outcomes.

Starting with a maximally-mixed initial state, we perform measurements of the bond operators. The plaquette operators, given by the product of bond operators around an elementary plaquette, are all measured after a short time $t_* \sim O(\log L)$, as we argue in Sec. III. Inspired by the solution of the Kitaev honeycomb model[27], we take the following ansatz to describe the density matrix of the Majorana fermions $\rho_f(t)$ for times $t > t_*$, before projecting back into the spin Hilbert space,

$$\rho_f(t) = \rho_c(t) \otimes \rho_b \quad (2)$$

Here, $\rho_b = |\Psi_b\rangle \langle \Psi_b|$ is a pure state in which each b Majorana fermion is “dimerized” with its nearest neighbor, i.e. so that $i b_r^j b_{r'}^j |\Psi_b\rangle = |\Psi_b\rangle$ where r, r' are lattice sites which are connected by a j -type bond with $j \in \{x, y, z\}$. This ansatz for the density matrix is particularly convenient since its form is preserved under the circuit dynamics: Note that any bond operator may be represented as the product of the four Majorana fermions along that bond. A measurement of this operator manifestly commutes with the density matrix ρ_b . As a result, these measurements give rise to dynamics of the c Majorana partons, while leaving the state of the b fermions invariant. It is also important to note that when we project the ansatz in Eq.(2) back into the Hilbert space of the spins, the resulting density matrix $\rho(t) = P\rho_f(t)P / \text{Tr}(P\rho_f)$ is stabilized by all of the plaquette operators so that $\text{Tr}(W_p \rho(t)) = 1$ ³. Therefore, the ansatz in Eq.(2) is only valid for $t > t_*$, when all plaquette operators have been measured and have definite values⁴.

A partial understanding of the steady-state entanglement properties of the monitored pure-states is obtained by taking the c Majorana partons to be in a pure state $|\Psi_c\rangle$ in which all of the Majoranas are “dimerized”, i.e. for each site r there is another site r' such that $i c_r c_{r'} |\Psi_c\rangle = \pm |\Psi_c\rangle$; the sign of the fermion parity will be unimportant for determining the entanglement properties of the steady-state. These operators can be visualized as forming a unique pairing of distinct sites on the honeycomb lattice which evolves under the monitored

³ The density matrix in Eq. (2) on the torus is also stabilized by the product of the bond operators around any non-contractible cycle of the torus. We will return to this point at the end of this section.

⁴ In general, when plaquette operators get measured by the circuit dynamics, their value is randomly set to be ± 1 , while for the ansatz in Eq.(2) all plaquette operators have value $+1$. This is not an issue because we are only interested in the entanglement properties of the resulting state which is independent of the sign of the stabilizers. Alternatively, one can choose the parity of $i b_r^j b_{r'}^j$ dimers in the ansatz (2) such that it results in correct signs for the plaquette stabilizers.

dynamics generated by the two-spin measurements. We may see this by considering a concrete example, which is summarized in Fig. 3a: let the pure state $|\Psi_c\rangle$ be given such that $ic_1c_{1'}|\Psi_c\rangle = ic_2c_{2'}|\Psi_c\rangle = 1$ where the sites 1 and 2 are nearest-neighbors connected by an y -type bond. The two-spin measurement $Y_1Y_2 = c_1b_1^yb_2^yc_2$ is now performed, yielding the outcome that $Y_1Y_2 = +1$. Applying the projection operator $\Pi \equiv (1 + c_1b_1^yb_2^yc_2)/2$

$$\begin{aligned} & \Pi \frac{1 + ic_1c_{1'}}{2} \frac{1 + ic_2c_{2'}}{2} \frac{1 + ib_1^yb_2^y}{2} \Pi \\ &= \frac{1 - ic_1c_2}{2} \frac{1 + ic_1c_{2'}}{2} \frac{1 + ib_1^yb_2^y}{2} \end{aligned} \quad (3)$$

yields the result that $-ic_1c_2$ and $ic_1c_{2'}$ are the new stabilizers for the evolving pure state of the c fermions. In terms of the original configuration, the endpoints of the two dimerized Majoranas have now been paired together as a result of the measurement.

The evolving density matrix for the original spins $\rho(t) \sim P\rho_f(t)P$ is stabilized by all elements of the stabilizer group of $\rho_f(t)$ which commute with P . Each Majorana dimer $ic_{\mathbf{r}}c_{\mathbf{r}'}$ stabilizing $\rho_f(t)$ gives rise to a stabilizer $W_{\mathbf{r}\mathbf{r}'}$ for $\rho(t)$, which is given, up to an overall sign, by the product of bond operators along any path connecting the two points, as shown in Fig. 3b. Physically, the c Majorana partons carry gauge charge, and must be connected by a Wilson line in the physical Hilbert space. The full entanglement structure of the steady state depends on the plaquette stabilizers W_p in addition to $W_{\mathbf{r}\mathbf{r}'}$ stabilizers.

B. Entanglement Properties of the Monitored Trajectories

For any qubit stabilizer wavefunction, the von Neumann entanglement entropy of a subsystem A is given by $S_A = -\text{Tr}[\rho_A \log_2 \rho_A] = I_A - |A|$ where $|A|$ is the number of qubits in the A subsystem and I_A counts the number of stabilizers which are linearly-independent, after restricting their support to the region A . Using this expression, we show in Appendix A that if the A subsystem is semi-infinite with a perfectly “flat” boundary that cuts across the z -type bonds of the honeycomb lattice, that the entanglement entropy of this region

$$S_A = \frac{n_p + n_\ell}{2} - 1 \quad (4)$$

where n_p is the number of plaquettes that cross the entanglement bipartition, and n_ℓ counts the number of string stabilizers $W_{\mathbf{r}\mathbf{r}'}$ which contain only one of their endpoints in the A subsystem (equivalently, the number of dimerized pairs of the c Majorana partons which cross the entanglement cut). Though the above expression is not exact when the boundary of the A subsystem is not perfectly flat, we conjecture that for any sufficiently large subsystem, that S_A and n_ℓ scale in the same way with subsystem size, up to area-law corrections.

The above relation may be used to determine the entanglement properties of the monitored pure-states as the relative measurement rates p_x, p_y, p_z are tuned. First, using (4), we argue on general grounds that when $p_x = p_y = p_z = 1/3$, the steady-state must exhibit topological order or super-area-law scaling of the entanglement entropy. Consider starting from a pure stabilizer state where all plaquette operators have been already measured and the rest of degrees of freedom are specified by a set of *short* string stabilizers $\{W_{\mathbf{r}\mathbf{r}'}\}$ between distinct pairs of lattice sites, e.g. when all links of a particular color, say red, have been measured. As the circuit dynamics changes the state, the collection of the string stabilizers $\{W_{\mathbf{r}\mathbf{r}'}\}$ evolves with time. In the steady-state, let $Q(r)$ be the probability distribution over the ensemble of monitored pure-states for a string stabilizer to connect two sites at a Cartesian distance r apart from each other⁵, meaning that for a given string stabilizer, the probability that the distance between its end points is between r and $r + dr$ is given by $Q(r)dr$. If the string stabilizers in the steady state are *short-ranged* so that the typical Cartesian distance between their endpoints $\int dr r Q(r) \sim \text{const.}$ in the thermodynamic limit, then $Q(r)$ must decay faster than r^{-2} at long distances. In this case it is meaningful to define the number of string stabilizers $W_{\mathbf{r}\mathbf{r}'}$ that pass through a cut that wraps around a cycle of the torus, i.e. when \mathbf{r} and \mathbf{r}' are on different sides of the cut. As we demonstrate in the Appendix B, the *number parity* of strings crossing such a cut is (i) preserved by the dynamical rules evolving a dimer configuration and (ii) the same for all other vertical cuts on the lattice. This number parity can be detected in the steady-state by an operator whose support extends along the cut and is localized in the direction transverse to the cut. Therefore, a short-ranged ensemble of string stabilizers in the steady-state implies that the dynamics at the isotropic point can encode non-local information about the initial state of the system, similar to a topological quantum order. On the other hand, if $Q(r) \sim r^{-\alpha}$ with $\alpha \leq 2$ at long distances, the typical string stabilizers are long-ranged, and the dimer number parity across a vertical cut becomes ill-defined. Note that in this case, since the string lengths could grow to be of the order of the system size, being on different sides of the cut is no longer well defined due to the periodic boundary conditions⁶. If one considers putting the system on an infinite cylinder instead, the number parity across a cut can be defined and it would be conserved, yet the operator that measures this quantity is no longer localized around the cut, but is extended across the system. However in this

⁵ On a torus, the Cartesian distance between two points is defined to be the length of the shortest path connecting the two.

⁶ One can define left and right sides of the cut as the regions of width $L/2$ on either side of the cut, but given that the strings are long-ranged, the number parity would no longer be conserved by the dynamics with this definition

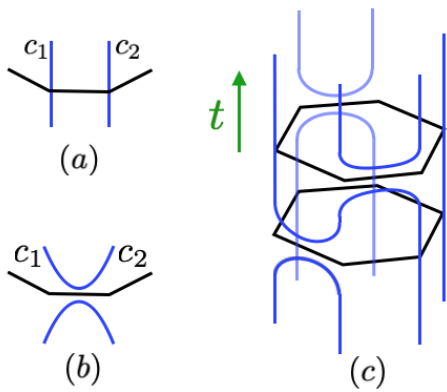


FIG. 4: **Loop Representation of the Stabilizer**

Evolution: The spacetime evolution of the string stabilizers $W_{rr'}$ can be understood by keeping track of their endpoints. A projective measurement of a bond operator leads to a dynamical rule that the loops incident upon the vertices of bond are connected, and a new pair of loops is sourced at the bond, as shown in (b). These endpoints evolve as in (a) when no measurement is performed. The collective evolution of these endpoints can be interpreted as a loop model on a bipartite, three-dimensional lattice, as shown in (c).

case, the system will exhibit super-area-law scaling of the entanglement entropy; since $Q(r) \sim r^{-\alpha}$ with $\alpha \leq 2$, given a disk of diameter ℓ , the contribution to the von Neumann entropy from string stabilizers which extend a distance larger than ℓ is $S_A \sim \ell^2 \int_{r \geq \ell} Q(r) dr \sim \ell^{3-\alpha}$.

In summary, we find on general grounds that either: a) the steady state encodes and preserves non-local information about the initial state similar to a topological quantum order or b) exhibits a super-area-law scaling of entanglement entropy. As we will see, both scenarios happen at different points in the phase diagram. It is worth noting that this line of argumentation and conclusion are reminiscent of a Lieb-Schultz-Mattis-Oshikawa-Hastings (LSMOH) theorem [19, 40, 50] for the nature of the ground-state in the Kitaev model in the presence of three-fold (C_3) rotational symmetry; in this case, since the C_3 symmetry anti-commutes with the parity of c Majorana partons, the ground state cannot be parity-symmetric and short-range entangled.

C. Loop Model representation of the Stabilizer evolution

A universal understanding of the entanglement properties of the steady-state may be obtained by studying the dynamics of the Majorana partons as the relative measurement rates p_x, p_y, p_z are tuned. Given the initial state (2), the bond measurements give rise to a free-fermion evolution of the c Majorana partons, as derived in Eq. (3). After projecting back into the spin Hilbert

space, each pair of dimerized partons can be viewed as forming the endpoints of a string which has zero line tension, due to the fact that all of the plaquette operators $\{W_p\}$ belong to the stabilizer group (the \mathbb{Z}_2 fluxes are pinned and static within the steady-state of each realization of the monitored evolution involving bond measurements). A spacetime representation of the evolving string operators $\{W_{rr'}\}$ may now be invoked, by keeping track of the evolving endpoints of each string stabilizer. The spacetime evolution of these endpoints trace out loops in three dimensions, as shown in Fig. 4. A projective measurement of a bond operator leads to the dynamical rule that the loops incident upon the vertices of the bond are connected and a new pair of loops are sourced at this bond, as shown in Fig. 4a and b. We note that this representation has been previously used to understand the free-fermion evolution of Majorana fermions in two spatial dimensions under frequent measurements [48], where it was shown that the spacetime evolution of the endpoints of the paired Majorana fermions leads to a representation of the ensemble of evolving pure-states of the Majorana fermions as a fully-packed loop model on a bipartite lattice in three dimensions.

A description of this loop model as a non-linear sigma model with target space CP^{n-1} and in the replica limit $n \rightarrow 1$ was studied in Ref. [45, 47] and it is known that this model supports two phases: one in which the loops behave as a Brownian walk, so that the probability distribution of the Cartesian distance between endpoints of a loop, denoted $Q(r)$, scales as $Q(r) \sim r^{-2}$ [46], and another phase in which the loops are “short” and $Q(r) \sim \exp(-r/\xi)$. Much is also known about the continuous phase transition separating these two phases [49]. In conjunction with Eq. (4), we then conjecture that the monitored pure-states exhibit either (i) logarithmic violation of area-law scaling of the entanglement $S_A \sim L_A \log L_A$ or (ii) area-law scaling $S_A \sim L_A$, respectively. Indeed, numerical simulations reveal two entanglement phases corresponding to cases (i) and (ii), confirming this conjecture. We note that while scaling (i) is typical in 2d Fermi liquids with a 1d Fermi surface, it is generally not possible in the presence of time-reversal and translation symmetry in the ground-state of the Kitaev honeycomb model⁷ (See also Appendix C). Finally, we note that when one of the probabilities is zero, e.g.

⁷ In the Kitaev honeycomb model, time-reversal symmetry can be chosen to act on the Majorana partons as $c_r \rightarrow \pm c_r$ where the sign depends on whether r belongs to the A or B sublattice of the honeycomb lattice, respectively [27], which requires that the Majorana partons can only hop between different sublattices. In the presence of translational symmetry, the Hamiltonian describing the Majorana partons in momentum space then takes the form $h(\mathbf{k}) = f_x(\mathbf{k})\tau^x + f_y(\mathbf{k})\tau^y$ where the τ Pauli matrices act in sublattice space, so that the dispersion vanishes when both $f_x(\mathbf{k}) = 0$ and $f_y(\mathbf{k}) = 0$. The solution to these equations generically gives a set of points in momentum space, as opposed to a gapless manifold of states, which would be required to obtain a logarithmic violation of area-law scaling of the entanglement.

$p_z = 0$, the two dimensional system is effectively comprised of L decoupled one-dimensional systems. The entanglement dynamics of each one-dimensional system can be mapped to a two-dimensional classical loop model (See Refs.[33, 48, 53] and Appendix D).

The area-law-entangled phase exhibits topological quantum order. The easiest way to see this is to observe that the probability of having a stabilizer which is given by the product of bond operators around a non-contractible cycle of the torus in the steady-state is exponentially small in the linear dimension of the system in the area-law-entangled phase. Starting with a maximally-mixed initial state and evolving the system in this phase, the time for this Wilson loop operator to be measured should then scale as $t_{\text{purif}} \sim O(\exp(L))$. The dynamics can then lead to a non-local encoding of information about the initial state which is exponentially long-lived.

Other universal entanglement properties of the critical and topologically-ordered phases, which follow from the two phases of the loop-model representation of the stabilizer evolution, (e.g. measures of long-ranged tripartite entanglement, the expectation values of Wilson loop operators, topological entanglement entropy) will be discussed in Sec. IV alongside numerical simulations of these dynamics.

III. PURIFICATION DYNAMICS

We now study the purification dynamics of the system, starting from a maximally-mixed initial state, $\rho_0 = 1/2^N \mathbb{1}$ with entanglement entropy $S(\rho_0) = N$, where $S(\rho) = -\text{Tr}[\rho \log_2 \rho]$ denotes the Von Neumann entanglement entropy. One can imagine that at the start each qubit of the system is entangled with a reference qubit in the environment, making up a Bell pair together. After tracing out all the reference qubits, one obtains the maximally-mixed initial density matrix $\rho_0 = 1/2^N \mathbb{1}$ on the system qubits. Due to the measurements involved in the circuit, the system would eventually purify the state, with $S(\rho) = 0$ after sufficiently long time, which corresponds to disentangling the system qubits from the reference qubits. As is shown in Refs.[16, 17], the measurement-induced entanglement phase transition manifests itself as a phase transition in the purification dynamics, meaning that different entanglement phases can be characterized by how long it takes the circuit to purify the state. As we will explain below, the same connection holds in our system. We will argue that one can use the classical 3D loop model picture to argue about the purification dynamics of the circuit. In particular, we show that when the loops in the loop model are long ranged, which correspond to the phase with $L_A \log L_A$ entanglement the system would purify in a time that is at most polynomial in system size, whereas when the loops are short, which corresponds to the phase with area law entanglement, it takes exponentially long time for the

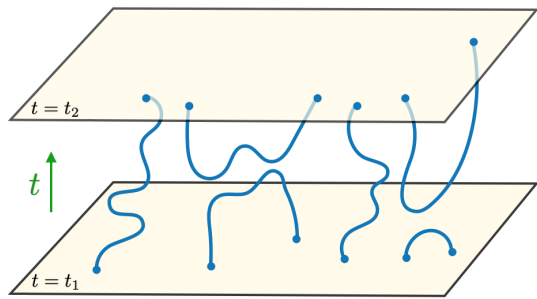


FIG. 5: **Spanning Number:** The purification dynamics of the bond operators may be understood by in the fully-packed loop model, by considering the number of strands of loops which connect an initial time t_1 to a final time t_2 . This *spanning number* decreases polynomially (exponentially) in $t_2 - t_1$ in the critical (topologically-ordered) phases.

circuit to completely purify the state (see Fig.6).

As we shall see, different degrees of freedom in the system get disentangled from the environment with different rates. Thus we start by identifying the degrees of freedom which are relevant to the purification dynamics. Consider the following set of commuting operators: 1) Plaquette operators, 2) the set of bond operators of a specific type, (e.g. z -type bond operators) and 3) the two long-cycle stabilizers, which are given by the product of bond operators along the non-trivial cycles of the torus (one horizontal and one vertical). It is easy to see that there are $L^2 - 1$ independent plaquette operators and $L^2 - 1$ independent z -bond operators in this set, and thus by including the two long cycle stabilizers, we have a complete set of $N = 2L^2$ commuting Pauli operators. Therefore, we may view the Hilbert space of the system as the tensor product of the Hilbert spaces of N virtual qubits consisted of $L^2 - 1$ plaquette qubits, $L^2 - 1$ bond qubits, and 2 long cycle qubits [68]. Accordingly, one can view the density matrix $\rho_0 = 1/2^N \mathbb{1}$, as the reduced density matrix of a larger state in which each virtual qubits makes a Bell pair with a corresponding reference qubit in the environment. Hence, the entanglement between the environment and the system can be viewed to be consisted of three different parts: 1) entanglement with the plaquette qubits, 2) entanglement with the bond qubits and 3) entanglement with the long cycle qubits. Below we discuss how each part gets disentangled from the reference system on the approach to the steady-state.

1. *Plaquette stabilizers:* Due to their local nature, the plaquette stabilizers are measured with constant relative rate for any point inside the phase diagram with $0 < p_x, p_y, p_z$ (see Appendix E for details). Hence, the entanglement entropy of the system will drop exponentially until $O(\log(L))$ times when all plaquettes are measured. This is true in both the topologically-ordered and the critical phase.

2. *Bond Operators:* The purification dynamics of the

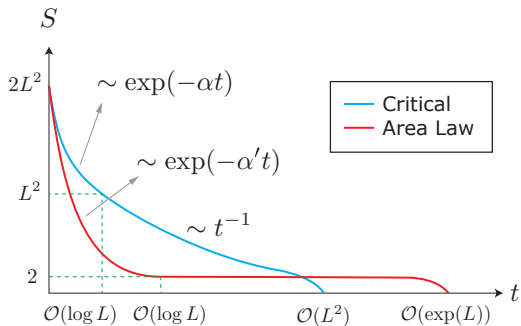


FIG. 6: **Purification Dynamics:** A summary of the evolution of the entropy of the system, starting from a maximally-mixed initial state in the critical phase (blue) and topologically-ordered phase (red).

bond qubits may be understood by starting with a density matrix for the Majorana partons

$$\rho_f \sim |\Psi_b\rangle \langle \Psi_b| \otimes \mathbf{1} \quad (5)$$

where $|\Psi_b\rangle$ describes a dimerized pure-state of the b Majorana fermions as described below Eq. (2). The corresponding density matrix for the spin degrees of freedom is volume-law-entangled, and is stabilized by all of the plaquette operators.

A subsequent measurement of a bond operator such as $X_{\mathbf{r}}X_{\mathbf{r}'}$ – where \mathbf{r} and \mathbf{r}' are adjacent sites separated by an x -type bond – is equivalent to adding $\pm ic_{\mathbf{r}}c_{\mathbf{r}'}$ as a stabilizer for the evolving state of the Majorana partons. We refer to $c_{\mathbf{r}}$ and $c_{\mathbf{r}'}$ as “paired” Majorana partons since they are now dimerized. The “unpaired” c Majorana partons each provide an $O(1)$ contribution to the entropy of the evolving state; once a bond operator connecting two such unpaired partons is measured, these degrees of freedom become “paired” and the entropy of the state decreases. In Appendix F, we show that the dynamics of these unpaired Majorana partons can be understood as a classical diffusion/annihilation reaction, in which the partons can take random steps whose lengths are power-law distributed in the critical phase. We show that this leads to a power-law decay of the entropy in the critical phase, as $S(t) \sim L^2/t$. As a result, it takes a polynomial time of $O(L^2)$ to disentangle the bond operators. On the other hand, the bond qubits will be disentangled exponentially fast in the topologically-ordered phase.

We note that an alternate understanding of the purification dynamics in the critical and topologically-ordered phases comes from the fully-packed loop model, which clarifies the universal nature of these dynamics in both phases. We again start from the state (5) of the parton degrees of freedom. This state may be viewed as the reduced density matrix of a pure-state in which each c Majorana parton has been dimerized with a reference Majorana degree of freedom. As a result, we may view each unpaired c Majorana parton as the endpoint of a loop which is attached to a reference Majorana. As the

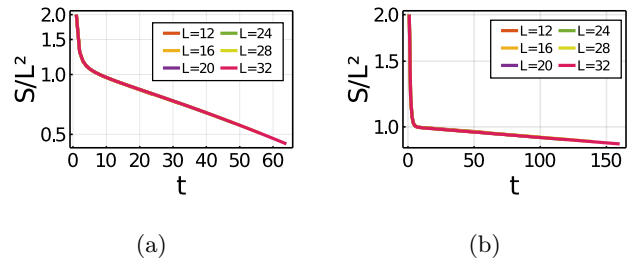


FIG. 7: **Purification of the Plaquette Stabilizers:** Entropy density as a function of time, starting from a totally mixed density matrix at (a) isotropic point $p_x = p_y = p_z = 1/3$ and (b) highly biased measurements with $p_x = p_y = 0.1$ and $p_z = 0.8$. The exponential decays in both plots are related to plaquette stabilizers being measured at constant rate.

measurements proceed, these loops evolve according to the rules presented in Sec. II B, and as shown schematically in Fig. 5. In a time-interval t , we may follow the spacetime trajectory of a loop; if the loop does not return to the initial time-slice within this interval, then the corresponding unpaired Majorana parton remains unpaired after time t , and contributes to the entropy of the system. Since each loop resembles a Brownian path in the critical phase, the motion of the loop in the time direction resembles a one-dimensional random walk. The probability that a given loop does not return to the initial interface is then given by the probability that a random walk on the interval $(0, t)$ initialized near the origin reaches the point t first, before reaching the origin. This probability decays as t^{-1} at long times [30]. From this reasoning, the entropy of the purifying state of the system may be identified with the *spanning number* of the loop model in a system with dimensions $L \times L \times t$, which counts the number of strands of loops which connect the bottom and top layers which are separated by a distance t . Since there are $O(L^2)$ such strands (one for each unpaired Majorana parton) in the initial time, the entropy should decay as L^2/t in the critical phase. In the topologically-ordered phase on the other hand, the spanning number decays exponentially in time, due to the exponentially small probability of having long loops [44].

3. *Long cycle stabilizers:* In the topologically-ordered phase, the long cycle stabilizers will remain entangled with reference qubits until times which are exponentially large in system size, as discussed in Sec. II A, due to the fact that in the topologically-ordered phase, the probability of having a long loop is exponentially small. In the critical phase, this entanglement survives only up to polynomial times.

The purification dynamics in both phases are summarized schematically in Fig. 6.

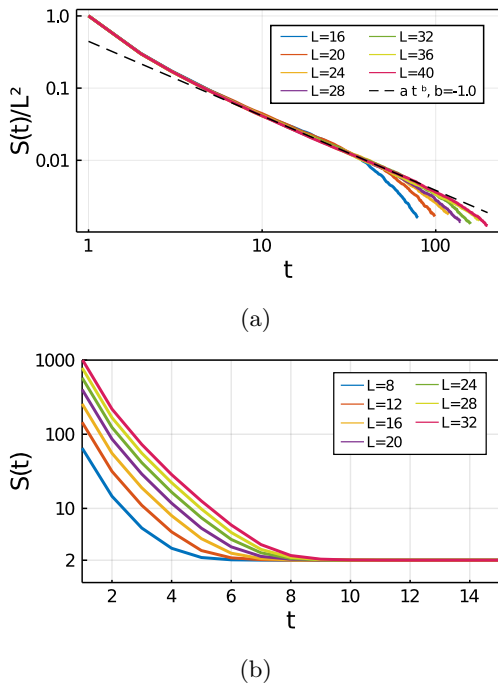


FIG. 8: **Purification of the Bond Operators** a) Entanglement entropy density versus time at the isotropic point $p_x = p_y = p_z$ and (b) Entanglement entropy versus time at $p_x = p_y = 0.1$ and $p_z = 0.8$. The initial state is the projection onto the subspace where all plaquette operators have definite values, say $+1$.

IV. NUMERICAL RESULTS

In this section, we numerically study the measurement-only dynamics considered in the previous section. The measurement-only dynamics here are studied in $L \times L$ systems with periodic boundary conditions, with $L \lesssim 40$ sites. Large-scale simulations of the monitored pure-states are made possible by the Clifford nature [15] of these dynamics, which permit an efficient storage of the evolving state of the spin degrees of freedom.

A. Purification Dynamics

We first numerically study the purification dynamics of the spins, starting from a maximally-mixed initial state. We observe that the plaquette stabilizers are added in a time $O(\log L)$ in both the topologically-ordered and critical phases, as shown in Fig. 7b and 7a, respectively. We note that starting with a maximally-mixed initial state, the rate at which plaquette stabilizers are being measured is very small; a plaquette stabilizer is added to the stabilizer group after the bond measurements are performed in a particular sequence around a given plaquette. As a result, the pre-factor appearing in the logarithmically-large timescale is quite large. For this reason, to study

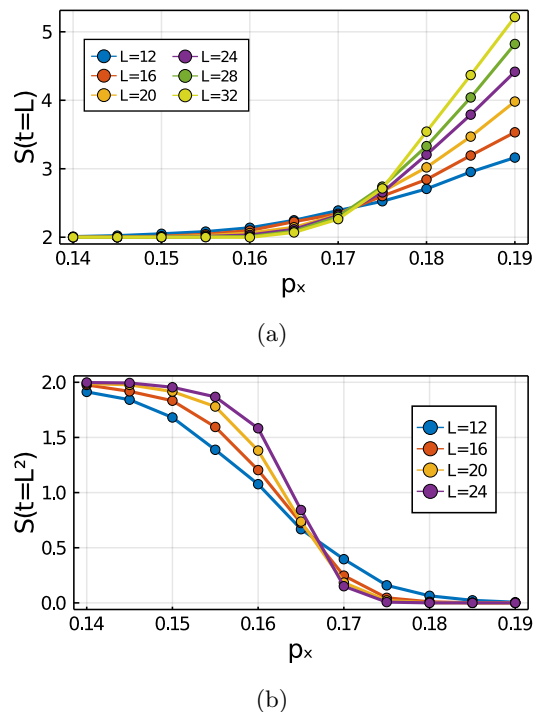


FIG. 9: Entropy of the purifying state of the system $S(t)$ for different values of p_x on the line $p_x = p_y$ at time (a) $t = L$ and (b) $t = L^2$.

the purification dynamics of the bond operators in the topologically-ordered and critical phases, we initialize the system in a state in which all of the plaquette stabilizers belong to the stabilizer group. The system still contains a finite entropy density. The reduction of the entropy of the system follows a power-law in time (Fig. 8a) in the critical phase. In contrast, the entropy of the system decreases exponentially in time in the topologically-ordered phase before saturating at 2 (Fig. 8b) for an exponentially long time before the system completely purifies. We can use the purifying dynamics as an order parameter to distinguish the topologically-ordered phase from the critical phase [16, 17]. To this end, we may look at $S(t)$ for $t = O(L)$, which is 2 in the topologically-ordered phase while it is $O(L)$ in the critical phase (see Fig. 9a). Otherwise, we can look at $S(t)$ at $T = O(L^2)$ which is 0 in the critical phase and 2 in the topologically-ordered phase (see Fig. 9b).

B. Scaling of subsystem entanglement entropy

We now study properties of the steady-state of the monitored dynamics. To study the properties of the steady-state, we measure all stabilizers (plaquettes and long cycle stabilizers) and all z -type bond operators. Then we run the circuit for $O(L)$ time step. We check the time dependence of the averaged quantities of interest to

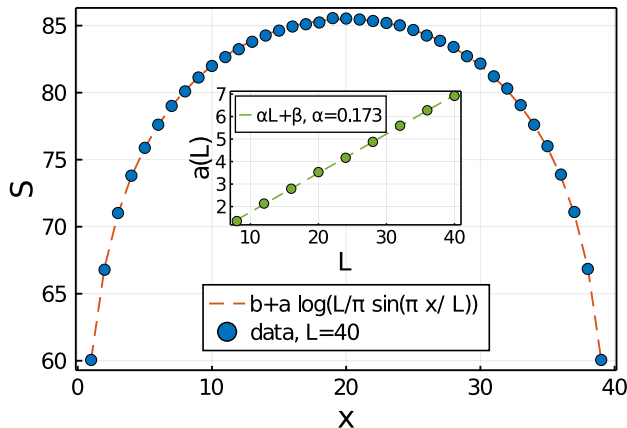


FIG. 10: **Entanglement in the Critical Phase.** Entanglement entropy of a cylindrical region of size $x \times L$ as a function of x for the steady state of the circuit at the point $p_x = p_y = p_z = 1/3$. The dashed line shows the best fit to the functional form in Eq. (6). The inset shows the best-fit value of the parameter $a(L)$ for different system sizes, which scales linearly in L .

make sure they are saturated by this time.

At the critical phase, we expect the string operators to have the length distribution of $1/l^2$ based on the 3D loop model. This in turns implies that the entanglement entropy of a subregion of linear size R should diverge as $R \log R$, for $R \ll L$ [48]. Fig. 10 shows the entanglement entropy of a cylindrical region as a function of its length x , at a fixed system size $L = 40$, at the isotropic point $p_x = p_y = p_z = 1/3$ after $t = L$ time steps. Fig. 32 in Appendix I shows the entanglement entropy of the cylinder of size $L/2$ as a function of time, to make sure the value we are reading is already saturated to its steady state value. As is clear from the Fig. 10, the entanglement entropy fits very well to the following,

$$S(x) = b(L) + a(L) \log \left[\frac{L}{\pi} \sin \left(\frac{\pi x}{L} \right) \right], \quad (6)$$

where $a(L)$ and $b(L)$ have been used as fitting parameters. Moreover, by changing the system size we find that the best fit parameter $a(L)$ scales linearly with system size as is shown in the inset of Fig.10. At the isotropic point, we find $a(L) = \alpha L + \beta$ with $\alpha \approx 0.173$, which results in a $\alpha L \log L$ leading term for scaling of the entanglement. Note that if we are at one of the percolation points, e.g. $(p_x, p_y, p_z) = (1/2, 1/2, 0)$, the system decouples into L 1d critical chains, resulting in the same $\alpha L \log L$ violation but with a prefactor $\alpha = \frac{\ln(2)\sqrt{3}}{2\pi} \approx 0.191$ [5, 48].

In general α seems to change inside the critical region. Moreover, it seems that it depends on the direction of the cylindrical region. Fig. 33a and Fig. 33b in Appendix I show the entanglement entropy of cylindrical regions with different cuts at the same point

$(p_x, p_y, p_z) = (0.2, 0.2, 0.6)$ which is still in the critical phase. As one can see, not only the value of α is different from that of the isotropic point, but its value also depends significantly on the configuration of the region, which shows that the steady state does not have rotational symmetry.

In the topologically-ordered phase, the entanglement entropy exhibits area-law-scaling as is expected from the the fact that the loops in the 3D loop model are short ranged in this phase. An example is shown in Fig. 34 in Appendix I for $(p_x, p_y, p_z) = (0.1, 0.1, 0.8)$.

C. Mutual Information

To detect the phase transition between the critical phase and the area law phase, we may look at how the information is shared between distant parts of the system. To this end, consider slicing the torus into four cylinders with equal length of $L/4$ as is shown in Fig. 11. A natural diagnostic for the phase transition between the topologically-ordered and critical phases is the mutual information between A and C [37]:

$$I_2(A : C) = S_A + S_C - S_{AC}. \quad (7)$$

$I_2(A : C)$ measures the correlations between the information in A and C . In terms of stabilizers of the state, $I_2(A : C)$ counts the number of independent stabilizers that have support only on A and C , but cannot be expressed as product of stabilizers which are supported only on A or C . Another measure used for detecting entanglement phase transition is the tripartite mutual information between A , B and C [67], which is defined as:

$$I_3(A : B : C) = I_2(A : B) + I_2(A : C) - I_2(A : BC) \quad (8)$$

$$= S_A + S_B + S_C - S_{AB} - S_{BC} - S_{AC} + S_{ABC}. \quad (9)$$

$I_3(A : B : C)$, when negative, is indicative of information shared between three regions that can only be inferred by having access to all three regions.

Fig. 14a shows $I_2(A : C)$ as a function of p_x on the symmetric line $p_x = p_y$. The initial state of the circuit has been chosen similar to that of Section IV B and mutual information is measured after $O(L)$ time steps. As is clear from Fig. 14a, $I_2(A : C) = 1$ throughout the area law phase. It is straightforward to understand this result in the limit that $p_x = p_y = 0$. The stabilizer group has a very simple form in this limit. Since $p_z = 1$, the stabilizer group of the state is generated by all the z bond operators, in addition to plaquette operators and the two long cycle stabilizers. Now consider the operator which is the product of all z bond operators with a non-trivial support in region B (shown as thick red lines in Fig.12) multiplied by plaquette operators in every other row of B (shaded plaquettes in Fig.12). This operator, which is a stabilizer of the state, acts trivially in B and only has

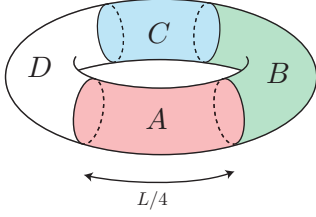


FIG. 11: The non-contractible regions A , B and C which are used for the calculation of the bipartite mutual information $I_2(A : C)$ and the tripartite mutual information $I_3(A : B : C)$ in Sec. IV C.

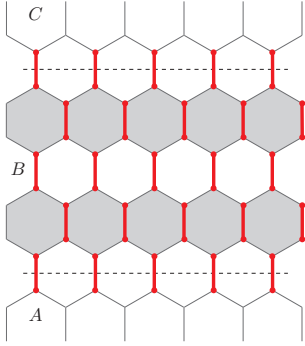


FIG. 12: The product of the red bond-operators and the shaded plaquette operators act trivially in B and only has support in A and C . This is the operator which results in $I(A : C) = 1$ in the limit that $p_x = p_y = 0$.

non-trivial support in A and C , while it can not be expressed as a product of stabilizers which are localized in either A or C . Hence it results in a unit mutual information between A and C . When $p_z < 1$ and p_x and p_y are finite, the generating set of the stabilizer group would be more complicated, but as is shown in Appendix G, a similar operator still exists in the stabilizer group, resulting in $I(A : C) = 1$.

On the other hand, in the critical phase, there are long range string operators spanning between A and C . A single string operator that goes from A to C does not contribute to $I_2(A : C)$ because it has non-trivial support on B as well. However, the product of any two string operators that span between A and C can be made to have a trivial support on B by multiplying it with appropriate plaquette operators inside B (See Appendix G for details) and hence contributes to $I(A : C)$. Therefore, one expects $I_2(A : C)$ to scale asymptotically as the number of independent string stabilizers that go from A to C , which itself increase with system size. The inset of Fig. 14a plots $I_2(A : C)$ as a function of system size L at the isotropic point $p_x = p_y = p_z$. It is clear from the inset plot that $I_2(A : C)$ scales linearly with L for large enough system sizes. This scaling can be easily under-

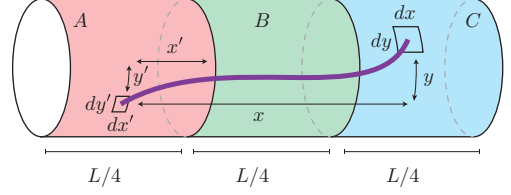


FIG. 13: Geometrical meaning of variables appearing in Eq.(11), to count the number of string operators that start in region A and end in region C

stood by computing the number of string operators going from A to C . Let

$$G(\mathbf{r})d\mathbf{a} \quad (10)$$

denote the probability that a string which starts at the origin, ends at an infinitesimal area element $d\mathbf{a}$ around position \mathbf{r} . Based on the loop model picture we have $G(\mathbf{r}) \sim 1/r^3$ at the isotropic point⁸ Therefore, the expected total number of strings with endpoints in A and C would be proportional to (see Fig.13):

$$I_2(A : C) \propto \int_{-L/2}^{L/2} dy' \int_0^{L/4} dx' \int_{-L/2}^{L/2} dy \int_{x'+L/4}^{x'+L/2} \frac{dx}{(x^2 + y^2)^{3/2}}. \quad (11)$$

As can be seen from dimensional analysis, this integral is proportional to L which explains the linear scaling of the mutual information shown in the inset of Fig. 14a⁹

Fig. 14b shows the tripartite mutual information $I_3(A : B : C)$ as a function of p_x on the symmetric line $p_x = p_y$. In the topologically-ordered phase, since the string operators are short ranged, the first and last terms in Eq. (8) cancel out and we find $I_3(A : B : C) = I_2(A : C) = +1$. However, deep in the critical phase, $I_2(A : BC)$ picks up a contribution from one string operator which spans the whole ABC interval and hence we get $I_3(A : B : C) = -1$. Note that while there are extensive number of strings that span the whole ABC , only one of them is *independently* shared between the three region. In other words, one can choose the generators of the stabilizer group of ρ_{ABC} such that all operators are localized on either AB , BC or AC regions except one

⁸ Note that the length probability distribution $Q(r)dr$ mentioned in Section II is given by the integral of $G(\mathbf{r})$ along a thin circular strip of radius r and hence is given by $Q(r) \sim 1/r^3 \times 2\pi r \sim 1/r^2$, assuming rotational symmetry of $G(\mathbf{r})$.

⁹ We note that $G(\mathbf{r}) \sim 1/r^3$ is only valid when $r \ll L$, so the above calculation should be seen as heuristic, not rigorous.

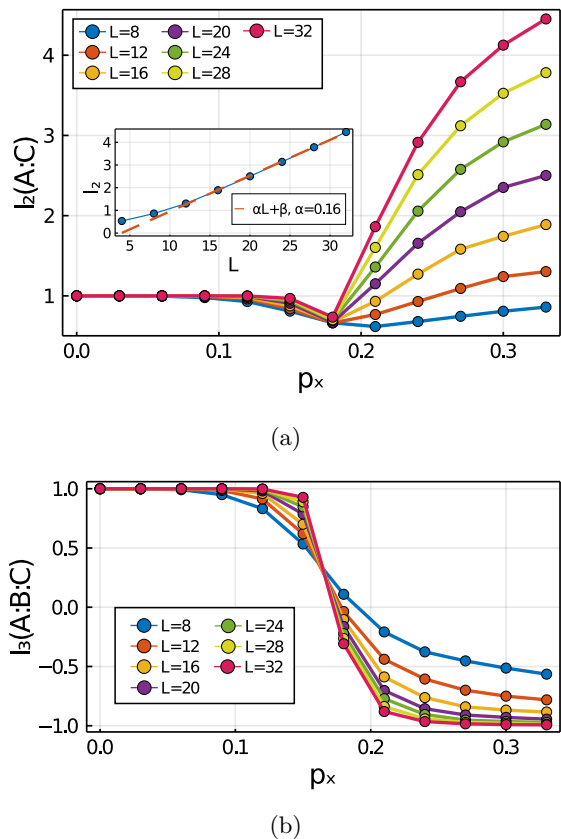


FIG. 14: Steady state mutual information between cylindrical regions (shown in Fig.11) versus p_x for points on the symmetric line $p_x = p_y$: (a) bipartite mutual information $I_2(A : C)$. The inset shows $I_2(A : C)$ at $p_x = p_y = 1/3$ versus system size L (b) Tripartite mutual information $I_3(A : B : C)$.

generator that spans the whole ABC region. This is because of the fact that the product of two string operators spanning the whole ABC region can be made to have trivial support on B by multiplying it with appropriate plaquette operators in B .

It is worth noting that in a 2d free Fermion system one would find the $L \log L$ violation of the area law as well as the linear scaling of mutual information, similar to what we observe in the critical phase of the circuit, while the tripartite mutual information for similar geometry vanishes, in contrast to the -1 value we find in the critical phase of our model. See Appendix C for more details.

We also contrast the behavior of $I_3(A : B : C)$ considered above with the topological entanglement entropy (TEE), which is equivalent to the tripartite mutual information between three contractible regions A, B, C arranged in a particular geometry (see [28, 36]), in which each region shares an edge with both of the remaining regions. To this end, we numerically investigate the behavior of the TEE of the steady state. We find that the TEE is always equal to 1 regardless of which phase we

are in (see Fig.35 in Appendix I), due to the fact that any monitored trajectory contains a frozen configuration of the \mathbb{Z}_2 fluxes and is thus stabilized by each of the plaquette operators. We note that the ground state of the Kitaev honeycomb model has also TEE equal to 1 in both the gapped phase and the gapless phase.

D. Wilson Line Correlators

Let $W_{\mathbf{r}\mathbf{r}'}$ denote the string operator which is composed of product of bond operators along a path which starts at site \mathbf{r} and ends at site \mathbf{r}' . We are interested in evaluating $\langle W_{\mathbf{r}\mathbf{r}'} \rangle^2$ in the steady state, where the line indicates an average over trajectories of the monitored dynamics using Born's rule. We note that $\langle W_{\mathbf{r}\mathbf{r}'} \rangle$ is always short-ranged due to the fact that each monitored pure-state hosts a random background of pinned \mathbb{Z}_2 fluxes. Since the monitored pure-state of the spins is always a stabilizer wavefunction, the quantity $\langle W_{\mathbf{r}\mathbf{r}'} \rangle^2$ is either $+1$ or 0 within any monitored trajectory, and $\langle W_{\mathbf{r}\mathbf{r}'} \rangle^2$ is proportional to the probability that the string operator connecting \mathbf{r} and \mathbf{r}' belongs to the stabilizer group of the steady state. Based on the symmetries of the ensemble of monitored trajectories, this probability is only a function of $\mathbf{r} - \mathbf{r}'$, hence we study

$$g(\mathbf{r} - \mathbf{r}') \equiv \overline{\langle W_{\mathbf{r}\mathbf{r}'} \rangle^2}. \quad (12)$$

Here we focus on the isotropic point $p_x = p_y = p_z = 1/3$, where we expect these correlations to only depend on the distance $|\mathbf{r} - \mathbf{r}'|$. We expect that for \mathbf{r} much greater than lattice spacing, $g(\mathbf{r})$ would have the same behaviour as $G(\mathbf{r})$ in Eq.(10).

Due to the particular nature of the circuit model, $g(\mathbf{r} - \mathbf{r}') = 0$ for any $|\mathbf{r} - \mathbf{r}'| = 2k$ with $k \in \mathbb{Z}$ at any time¹⁰. At the isotropic point $p_x = p_y = p_z = 1/3$, these correlations only depend on the graph distance $|\mathbf{r} - \mathbf{r}'|$. Fig. 15 shows $g(\mathbf{r})$ for $r = 2k + 1$ at the isotropic point. We observe that this quantity falls as a power law $\sim r^{-\Delta}$, with an exponent $\Delta \approx 2.9$ until $r \sim L/2$ where it flattens. This agrees with $G(\mathbf{r}) \sim 1/r^3$ scaling from the loop model picture.

E. Phase Transition

If the point at $p_x \hat{x} + p_y \hat{y} + p_z \hat{z}$ corresponds to the circuit parameters (p_x, p_y, p_z) , the phase diagram consists of the points inside a equilateral triangle whose three vertices lie at \hat{x}, \hat{y} and \hat{z} (see Fig.1). Based on the symmetries of the circuit model, the phase diagram should be symmetric under rotations around the center of the triangle by

¹⁰ in an abuse of notation, we use $|\mathbf{r} - \mathbf{r}'|$ to denote the graph distance between \mathbf{r} and \mathbf{r}' , i.e. the minimum number of edges on the Honeycomb lattice one should cross to go from \mathbf{r} to \mathbf{r}'

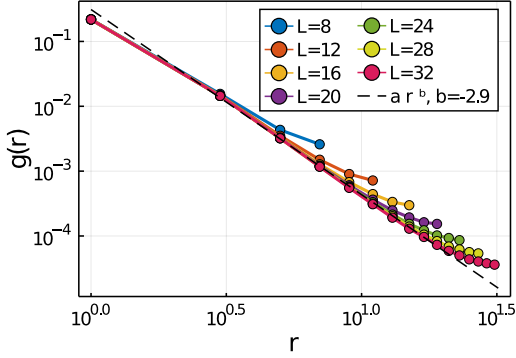


FIG. 15: The expectation value $g(r) \equiv \overline{\langle W_{\mathbf{r}\mathbf{r}'} \rangle^2}$ as a function of $r \equiv |\mathbf{r} - \mathbf{r}'|$ at the isotropic point $p_x = p_y = p_z$. The dashed line is the best power law fit for system size $L = 32$, which is consistent with analytic predictions.

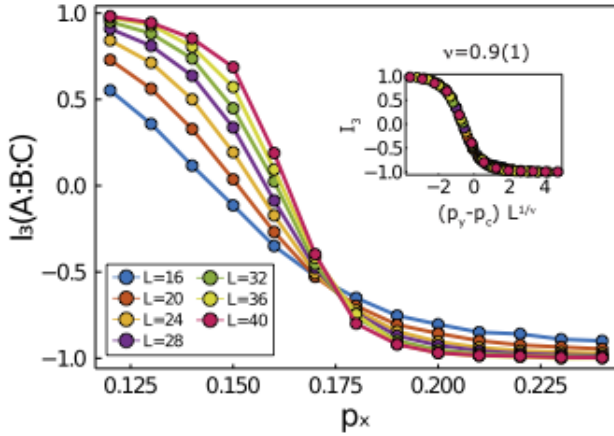


FIG. 16: The tripartite mutual information of the steady state versus p_x on the symmetric line $p_x = p_y$, near the phase transition at $p_c = 0.172(5)$. The inset shows the data collapse of the same data using the scaling form of Eq.(13) with $\nu = 0.9(1)$.

$\theta = 2\pi/3$ as well as reflections about the perpendicular bisector of each sides. We may use this symmetries to simplify mapping out the phase diagram.

To map out the phase diagram and determine the critical exponents associated with the corresponding phase transition, we make use of the tripartite mutual information $I_3(A : B : C)$ defined above, using the same partitioning of the torus as in Fig. 11.

Fig. 16 shows $I_3(A : B : C)$ as a function of $p_y = p_x$ in the vicinity of the phase transition. We choose sections A , B and C such that their boundary cut through the z -bonds. On general grounds, we may assume that I_3 follows the scaling form

$$I_3(p, L) = F((p - p_c)L^{1/\nu}), \quad (13)$$

where ν is the correlation length critical exponent. By collapsing the data according to this scaling form, we find $p_c = 0.172(5)$ and $\nu = 0.9(1)$.

By fixing p_x and varying p_y we can map out the whole phase diagram. Fig. 1 shows the result. The black dots are found via numerical simulation (see Fig.36 in the Appendix for the corresponding plots) while the white dots are just the symmetric counter parts of the black dots. The black squares on the sides correspond to 2D percolation fixed points. The three green regions are area law phases while the middle phase C correspond to the critical phase with $L \log L$ violation of entanglement entropy. Based on the numerical results it seems that the phase boundary corresponds to the incircle of the triangular phase diagram although this needs further investigation. Along the phase boundary the numerical estimate for the value of ν changes between 0.7 to 0.9 but the variation is inside the margin of error. On the other hand, for the 2D percolation fixed points on the boundary, we have $\nu = 4/3$.

V. PERTURBATIONS TO THE CRITICAL AND TOPOLOGICALLY-ORDERED PHASES

In this section, we consider perturbing away from the limit in which only bond operator measurements are performed in the monitored evolution, by adding in other kinds of measurements which have the effect of (i) removing the extensive number of conserved quantities in the dynamics considered previously and (ii) preventing a free-fermion description of the effective dynamics of the Majorana partons. We find that the critical and topologically-ordered phases remain stable.

In particular, we consider two different types of perturbations to the circuit dynamics. First we study the effect of adding random single qubit measurements. In particular, we consider a circuit model where at each step a random qubit is measured in the Z basis with probability p_s or a bond operator is measured at random with probability $(1-p_s)$ such that $p_s + (1-p_s)(p_x + p_y + p_z) = 1$. As we will argue in the following, we expect both phases to be stable for small enough values of p_s . To see this, it is helpful to consider the effect of this perturbation on a slightly modified circuit model first. Assume that we measure all the plaquette operators after each measurement of either bond operators or of single qubit operators. Note that when $p_s = 0$, measuring plaquette operators has no effect, since in the original model all of plaquette operators already belong to the stabilizer group of the steady state.

Now let us see how the stabilizer group changes when a single qubit measurement is performed. Imagine the qubit denoted by the red dot in Fig. 17 is measured in the Z basis. First we note that we can choose all of the string stabilizers such that they all commute with the Z measurement on the red qubit. To this end, we may choose the string operator which ends on the red qubit to pass through the z -bond emanating from the

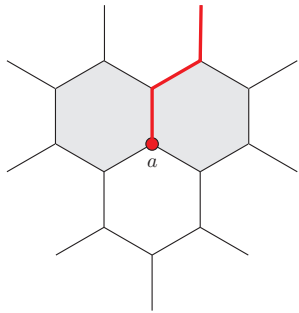
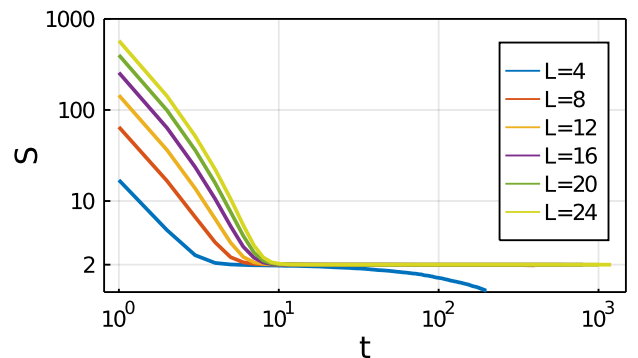


FIG. 17: We may choose all string operators such that all commute with a given single qubit measurement. For example, in the shown example, if we choose the string operator that ends on site a to come through the vertical z -bond, it will commute with the Z_a measurement.

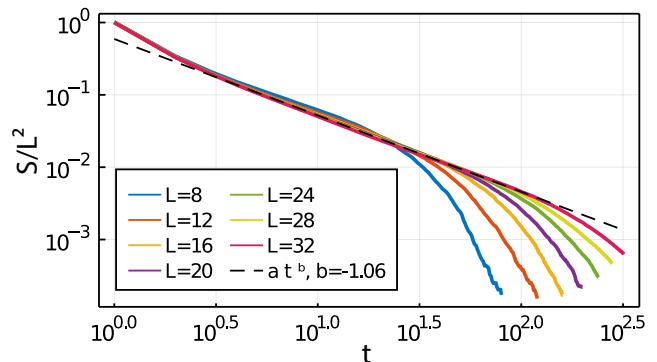
red dot, and we may choose the other string operators such that none have support on the red qubit. With this choice of generators for the stabilizer group, it is clear that after the single qubit measurement, the only change in the stabilizer group would be, (i) the single-qubit Z operator is added to the stabilizer group, and (ii) the two shaded plaquette operators in Fig. 17 are replaced by their product. As such, single qubit measurements pin the endpoints of string operators ending at these sites in particular directions, which should not change the long-distance properties of the length distribution $Q(r)$ of stabilizer endpoints. It is also clear that a subsequent measurement of all plaquette operators, will undo the effect of the Z measurement. so for any p_s we find the exact same phase diagram. Now let us relax the assumption of measuring all plaquette operators at each timestep of the circuit. Instead we assume that plaquette operators are measured randomly with probability p_{plq} , such that $p_s + p_{\text{plq}} + (1 - p_s - p_{\text{plq}})(p_x + p_y + p_z) = 1$. Based on the above arguments, one would expect to find the same phase diagram even in this model, as long as $p_s \ll p_{\text{plq}}$. This is indeed consistent with what we observe in numerical simulations.

Fig. 18a shows the purification dynamics of the system, starting from a maximally-mixed initial state, when $p_x = p_y = 0.1$ with perturbation parameters $p_s = 0.01$ and $p_{\text{plq}} = 0.1$. As is clear from the figure, the long cycle stabilizers remain entangled to the environment until long times, while the remaining of degrees of freedom rapidly disentangle, as was observed to be the case when $p_s = 0$. Moreover, TEE and $I_3(A : B : C)$ also remain equal to $+1$ for large system sizes as shown in Fig. 19a and Fig. 19b respectively.

Fig. 18b on the other hand corresponds to the purification dynamics when $p_x = p_y = p_z = 1/3$, with $p_s = 0.01$ and $p_{\text{plq}} = 0.1$, again showing a power-law decay of the entropy density as a function of time. The steady-state entanglement entropy also shows $S_A \sim L_A \log L_A$ scaling, as seen in Fig. 20 and the Wilson line correlation



(a)



(b)

FIG. 18: Purification dynamics in the presence of additional single-qubit measurements with $p_s = 0.01$ and $p_{\text{plq}} = 0.1$. Subplot (a) correspond to perturbing an area law point with $p_x = p_y = 0.1$ and subplot (b) corresponds to perturbing the isotropic point $p_x = p_y = p_z$, as described in the text.

$g(r)$ defined in Section IV D also decays as a power law $1/r^\Delta$ with $\Delta \sim 3$ as shown in Fig. 21. On the other hand, we find that TEE computed via the Kitaev-Preskill construction is no longer equal to 1 but it rather grows slowly with the system size as shown in Fig. 19c; we note, however, that the interpretation of the TEE for a super-area-law-entangled phase is not clear, and need not be a universal constant as it is in an area-law-entangled phase. Similarly, as can be seen in Fig. 19d the tripartite mutual information $I_3(A : B : C)$ is also no longer fixed at -1 , but rather scales linearly with the system size. Note that the argument we provide in Section IV C for $I_3(A : B : C) = -1$ fails in the presence of single-qubit measurements. For every single-qubit measurement performed near the boundary of AB , the product of plaquette operators spanning the boundary becomes part of the stabilizer group. As a result, the product of a typical pair of string operators spanning ABC cannot necessarily be reduced in its support, by the action of elements of the stabilizer group, to an operator supported exclusively on A and C . From the distribution $Q(r) \sim r^{-2}$ in

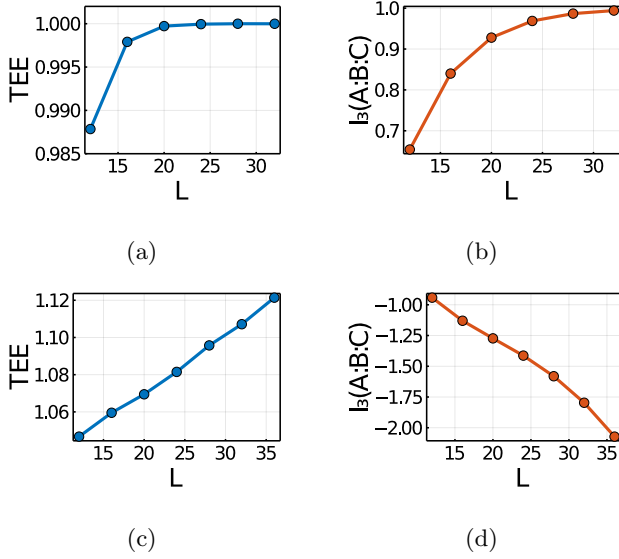


FIG. 19: (a) TEE and (b) tripartite mutual information versus system size in the steady state of an area law point with $p_x = p_y = 0.1$ perturbed with $p_{\text{plq}} = 0.1$ and $p_s = 0.01$. (c) and (d) show analogous quantities when the same perturbation is applied to the isotropic point $p_x = p_y = p_z$.

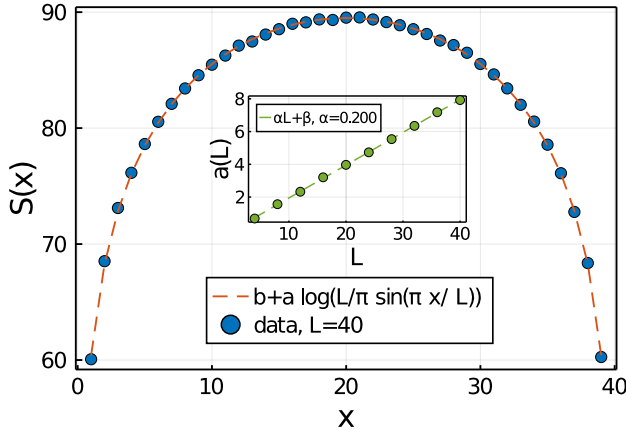


FIG. 20: Entanglement entropy of a cylindrical region of size $x \times L$ as a function of x for the steady state of the circuit at the isotropic point $p_x = p_y = p_z$ perturbed with $p_s = 0.01$ and $p_{\text{plq}} = 0.1$.

the critical phases, there should be $O(L)$ such long stabilizers spanning the ABC region, which gives rise to the behavior in Fig. 19d.

Finally, let consider perturbing the original circuit model. So now, at each step, a random qubit would be measured with probability p_s , or a bond operator would be measured with probability $(1 - p_s)$ such that $p_s + (1 - p_s)(p_x + p_y + p_z) = 1$. As we have discussed before, plaquette operators are still being measured with

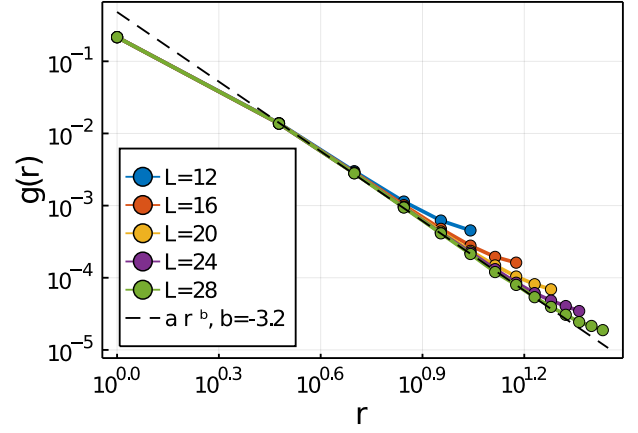


FIG. 21: The Wilson line correlation $g(r)$ in the steady state of the isotropic point $p_x = p_y = p_z$ perturbed with $p_s = 0.01$ and $p_{\text{plq}} = 0.1$.

constant rate, say q , due to the bond operator measurements, though we no longer measure the plaquette operators directly. Therefore, based on the discussion so far, we expect both phases survive as long as $p_s \ll q$. Because q is very small in our model (see Fig. 39b in Appendix I), one has to go to very large system sizes to numerically verify this statement. Instead, we provide a more detailed argument in Appendix H to support this claim. On the other hand, when $p_s \gg q$, we observe that the monitored trajectories of the system settle into a volume law phase (see Fig. 38 in Appendix I).

Another way of perturbing the original dynamics is to add three-qubit measurements, given by the product of adjacent bond operators; this kind of perturbation, however, preserves both the free-fermion nature of the parton dynamics, while also keeping the extensive number of conservation laws. In the Majorana parton picture it translates into next nearest neighbour coupling of c Majoranas, which in turn translates into next nearest neighbour moves in the classical loop model. From the classical model, we know such a system would flow into another critical phase with long range correlations. This is indeed what we observe by numerically simulating the quantum circuit, where at a each step either a product of two adjacent bond operators is measured randomly with probability p_3 or a random bond operator is measured with probability $(1 - p_3)$. The entanglement entropy scaling in the steady state are shown for $p_3 = 0.5$ in Fig. 37a and for $p_3 = 0.1$ in Fig. 37b in Appendix I. The entanglement entropy clearly follows a $L \log L$ scaling with a p_3 dependent coefficient.

VI. DISCUSSION AND OUTLOOK

In this work, we studied how random measurements of non-commutative observables could give rise to non-

equilibrium phases of matter which exhibit long-range entanglement. While these dynamical entanglement phases of matter share some properties with their equilibrium counterparts like spin liquids, they can in principle exhibit novel features which can only appear in the non-equilibrium setting.

An interesting aspect of this work that warrants further investigation, is whether the out-of-equilibrium parton construction introduced here can be used to investigate other regimes of monitored evolution which give rise to long-range-entangled steady-states. Furthermore, it is important to understand the quantum error correction properties of the area law phase, which are closely related to the recent development of Floquet codes [18, 20, 51, 62]. As shown in Section III, when the measurement probabilities are highly biased, the random dynamics give rise to two dynamically generated logical qubits, which would be absent if one interprets the bond operators as gauge operators of a subsystem quantum error correcting code. However, it is not yet clear to what extent the area law phase could be used as a quantum error correcting code. In particular, it would be interesting to see whether this model has an efficient decoder with a finite threshold. Note that due to the random and indirect measurement of the stabilizer, the syndrome data of the dynamically generated code lacks structures like \mathbb{Z}_2 gauge symmetry, which should be trivially present in the standard surface code syndrome data. On the other

hand, the randomness might help the decoder to be more resilient against adversarial errors, compared to simpler models like the Floquet honeycomb code [18, 20].

Note Added: During completion of this work, we were made aware of forthcoming work [58] on a related problem.

ACKNOWLEDGMENTS

We thank Matthew P. A. Fisher, Yuan-Ming Lu, Ashvin Vishwanath, and especially Adam Nahum for useful discussions. SV gratefully acknowledges support from the Simons Center for Geometry and Physics, Stony Brook University at which some of the research for this paper was performed. ZXL is supported by the Simons Collaborations on Ultra-Quantum Matter, grant 651457 from the Simons Foundation. AL is supported by Joint Quantum Institute Physics Frontier Center at University of Maryland (JQI-PFC-UMD). This research was supported in part by the Heising-Simons Foundation, the Simons Foundation, and National Science Foundation Grant No. NSF PHY-1748958. We acknowledge the University of Maryland supercomputing resources (<http://hpcc.umd.edu>) made available for conducting the research reported in this paper. The numerical simulations in this study were partially conducted utilizing the QuantumClifford.jl package.

-
- [1] Ehud Altman, Kenneth R Brown, Giuseppe Carleo, Lincoln D Carr, Eugene Demler, Cheng Chin, Brian Demarco, Sophia E Economou, Mark A Eriksson, Kai-Mei C Fu, et al. Quantum simulators: Architectures and opportunities. *PRX Quantum*, 2(1):017003, 2021.
 - [2] P. W. Anderson. The resonating valence bond state in $\text{La}_{2-x}\text{Ce}_x\text{CuO}_4$ and superconductivity. *Science*, 235(4793):1196–1198, 1987.
 - [3] P.W. Anderson. Resonating valence bonds: A new kind of insulator? *Materials Research Bulletin*, 8(2):153–160, 1973.
 - [4] Pasquale Calabrese and John Cardy. Entanglement entropy and quantum field theory. *Journal of statistical mechanics: theory and experiment*, 2004(06):P06002, 2004.
 - [5] John Cardy. Conformal invariance and percolation. *arXiv preprint math-ph/0103018*, 2001.
 - [6] JT Chalker, N Read, V Kagalovsky, B Horovitz, Y Avishai, and AWW Ludwig. Thermal metal in network models of a disordered two-dimensional superconductor. *Physical Review B*, 65(1):012506, 2001.
 - [7] Bin Chen, Lin Chen, Peng-xiang Hao, and Jiang Long. On the mutual information in conformal field theory. *Journal of High Energy Physics*, 2017(6):1–37, 2017.
 - [8] Xiao Chen, Gil Young Cho, Thomas Faulkner, and Eduardo Fradkin. Scaling of entanglement in 2+1-dimensional scale-invariant field theories. *Journal of Statistical Mechanics: Theory and Experiment*, 2015(2):P02010, 2015.
 - [9] Soonwon Choi, Yimu Bao, Xiao-Liang Qi, and Ehud Altman. Quantum error correction in scrambling dynamics and measurement-induced phase transition. *Physical Review Letters*, 125(3):030505, 2020.
 - [10] Stefan Depenbrock, Ian P. McCulloch, and Ulrich Schollwöck. Nature of the spin-liquid ground state of the $s = 1/2$ heisenberg model on the kagome lattice. *Phys. Rev. Lett.*, 109:067201, Aug 2012.
 - [11] Veit Elser. Nuclear antiferromagnetism in a registered ^3He solid. *Phys. Rev. Lett.*, 62:2405–2408, May 1989.
 - [12] Ruihua Fan, Sagar Vijay, Ashvin Vishwanath, and Yi-Zhuang You. Self-organized error correction in random unitary circuits with measurement. *Physical Review B*, 103(17):174309, 2021.
 - [13] David Fattal, Toby S Cubitt, Yoshihisa Yamamoto, Sergey Bravyi, and Isaac L Chuang. Entanglement in the stabilizer formalism. *arXiv preprint quant-ph/0406168*, 2004.
 - [14] Lukasz Fidkowski, Jeongwan Haah, and Matthew B Hastings. How dynamical quantum memories forget. *Quantum*, 5:382, 2021.
 - [15] Daniel Gottesman. *Stabilizer codes and quantum error correction*. California Institute of Technology, 1997.
 - [16] Michael J Gullans and David A Huse. Dynamical purification phase transition induced by quantum measurements. *Physical Review X*, 10(4):041020, 2020.
 - [17] Michael J Gullans and David A Huse. Scalable probes of measurement-induced criticality. *Physical review letters*, 125(7):070606, 2020.

- [18] Jeongwan Haah and Matthew B Hastings. Boundaries for the honeycomb code. *Quantum*, 6:693, 2022.
- [19] Matthew B Hastings. Lieb-schultz-mattis in higher dimensions. *Physical review b*, 69(10):104431, 2004.
- [20] Matthew B. Hastings and Jeongwan Haah. Dynamically Generated Logical Qubits. *Quantum*, 5:564, October 2021.
- [21] Wen-Jun Hu, Shou-Shu Gong, Wei Zhu, and D. N. Sheng. Competing spin-liquid states in the spin- $\frac{1}{2}$ heisenberg model on the triangular lattice. *Phys. Rev. B*, 92:140403, Oct 2015.
- [22] Matteo Ippoliti, Michael J. Gullans, Sarang Gopalakrishnan, David A. Huse, and Vedika Khemani. Entanglement phase transitions in measurement-only dynamics. *Phys. Rev. X*, 11:011030, Feb 2021.
- [23] Yasir Iqbal, Federico Becca, and Didier Poilblanc. Projected wave function study of z_2 spin liquids on the kagome lattice for the spin- $\frac{1}{2}$ quantum heisenberg antiferromagnet. *Phys. Rev. B*, 84:020407, Jul 2011.
- [24] Yasir Iqbal, Wen-Jun Hu, Ronny Thomale, Didier Poilblanc, and Federico Becca. Spin liquid nature in the heisenberg $J_1 - J_2$ triangular antiferromagnet. *Phys. Rev. B*, 93:144411, Apr 2016.
- [25] Hong-Chen Jiang, Zhenghan Wang, and Leon Balents. Identifying topological order by entanglement entropy. *Nature Physics*, 8(12):902–905, 2012.
- [26] Ryui Kaneko, Satoshi Morita, and Masatoshi Imada. Gapless spin-liquid phase in an extended spin 1/2 triangular heisenberg model. *Journal of the Physical Society of Japan*, 83(9):093707, 2014.
- [27] Alexei Kitaev. Anyons in an exactly solved model and beyond. *Annals of Physics*, 321(1):2–111, 2006. January Special Issue.
- [28] Alexei Kitaev and John Preskill. Topological entanglement entropy. *Physical review letters*, 96(11):110404, 2006.
- [29] Johannes Knolle, Roderich Moessner, and Natalia B Perkins. Bond-disordered spin liquid and the honeycomb iridate $\text{h}_3\text{liir}_2\text{o}_6$: Abundant low-energy density of states from random majorana hopping. *Physical review letters*, 122(4):047202, 2019.
- [30] Pavel L Krapivsky, Sidney Redner, and Eli Ben-Naim. *A kinetic view of statistical physics*. Cambridge University Press, 2010.
- [31] Ville Lahtinen, Andreas W. W. Ludwig, and Simon Trebst. Perturbed vortex lattices and the stability of nucleated topological phases. *Phys. Rev. B*, 89:085121, Feb 2014.
- [32] Nicolai Lang and Hans Peter Büchler. Entanglement transition in the projective transverse field ising model. *Phys. Rev. B*, 102:094204, Sep 2020.
- [33] Ali Lavasani, Yahya Alavirad, and Maissam Barkeshli. Measurement-induced topological entanglement transitions in symmetric random quantum circuits. *Nature Physics*, 17(3):342–347, Jan 2021.
- [34] Ali Lavasani, Yahya Alavirad, and Maissam Barkeshli. Topological order and criticality in $(2 + 1)\text{D}$ monitored random quantum circuits. *Phys. Rev. Lett.*, 127:235701, Dec 2021.
- [35] P. Lecheminant, B. Bernu, C. Lhuillier, L. Pierre, and P. Sindzingre. Order versus disorder in the quantum heisenberg antiferromagnet on the kagomé lattice using exact spectra analysis. *Phys. Rev. B*, 56:2521–2529, Aug 1997.
- [36] Michael Levin and Xiao-Gang Wen. Detecting topological order in a ground state wave function. *Physical review letters*, 96(11):110405, 2006.
- [37] Yaodong Li, Xiao Chen, and Matthew PA Fisher. Measurement-driven entanglement transition in hybrid quantum circuits. *Physical Review B*, 100(13):134306, 2019.
- [38] Yaodong Li and Matthew PA Fisher. Statistical mechanics of quantum error correcting codes. *Physical Review B*, 103(10):104306, 2021.
- [39] Yaodong Li, Sagar Vijay, and Matthew Fisher. Entanglement domain walls in monitored quantum circuits and the directed polymer in a random environment. *arXiv preprint arXiv:2105.13352*, 2021.
- [40] Elliott Lieb, Theodore Schultz, and Daniel Mattis. Two soluble models of an antiferromagnetic chain. *Annals of Physics*, 16(3):407–466, 1961.
- [41] Yuan-Ming Lu, Ying Ran, and Patrick A. Lee. z_2 spin liquids in the $s = \frac{1}{2}$ heisenberg model on the kagome lattice: A projective symmetry-group study of schwinger fermion mean-field states. *Phys. Rev. B*, 83:224413, Jun 2011.
- [42] Ralf Metzler, Aleksei V Chechkin, and Joseph Klafter. Lévy statistics and anomalous transport: Lévy flights and subdiffusion. *arXiv preprint arXiv:0706.3553*, 2007.
- [43] Olexei Motrunich, Kedar Damle, and David A Huse. Particle-hole symmetric localization in two dimensions. *Physical Review B*, 65(6):064206, 2002.
- [44] Adam Nahum. *Critical phenomena in loop models*. Springer, 2014.
- [45] Adam Nahum, JT Chalker, P Serna, M Ortuno, and AM Somoza. 3d loop models and the cp_{n-1} sigma model. *Physical review letters*, 107(11):110601, 2011.
- [46] Adam Nahum, JT Chalker, P Serna, M Ortuno, and AM Somoza. Length distributions in loop soups. *Physical review letters*, 111(10):100601, 2013.
- [47] Adam Nahum, P Serna, AM Somoza, and M Ortuno. Loop models with crossings. *Physical Review B*, 87(18):184204, 2013.
- [48] Adam Nahum and Brian Skinner. Entanglement and dynamics of diffusion-annihilation processes with majorana defects. *Physical Review Research*, 2(2):023288, 2020.
- [49] M Ortuno, AM Somoza, and JT Chalker. Random walks and anderson localization in a three-dimensional class c network model. *Physical review letters*, 102(7):070603, 2009.
- [50] Masaki Oshikawa. Topological approach to luttinger’s theorem and the fermi surface of a kondo lattice. *Physical Review Letters*, 84(15):3370, 2000.
- [51] Adam Paetznick, Christina Knapp, Nicolas Delfosse, Bela Bauer, Jeongwan Haah, Matthew B Hastings, and Marcus P da Silva. Performance of planar floquet codes with majorana-based qubits. *arXiv preprint arXiv:2202.11829*, 2022.
- [52] Subir Sachdev. Kagomé- and triangular-lattice heisenberg antiferromagnets: Ordering from quantum fluctuations and quantum-disordered ground states with unconfined bosonic spinons. *Phys. Rev. B*, 45:12377–12396, Jun 1992.
- [53] Shengqi Sang and Timothy H. Hsieh. Measurement-protected quantum phases. *Phys. Rev. Research*, 3:023200, Jun 2021.
- [54] Lucile Savary and Leon Balents. Quantum spin liquids: a review. *Reports on Progress in Physics*, 80(1):016502,

nov 2016.

- [55] Chris N. Self, Johannes Knolle, Sofyan Iblisdir, and Jiannis K. Pachos. Thermally induced metallic phase in a gapped quantum spin liquid: Monte carlo study of the kitaev model with parity projection. *Phys. Rev. B*, 99:045142, Jan 2019.
- [56] Pablo Serna. 3d unoriented loop models and the $\mathbb{R}P^{n-1}$ sigma model. *arXiv preprint arXiv:2107.13366*, 2021.
- [57] Rajiv R. P. Singh and David A. Huse. Ground state of the spin-1/2 kagome-lattice heisenberg antiferromagnet. *Phys. Rev. B*, 76:180407, Nov 2007.
- [58] Aditya Sriram, Tibor Rakovszky, Vedika Khemani, and Matteo Ippoliti. *To appear*, 2022.
- [59] Martin Suchara, Sergey Bravyi, and Barbara Terhal. Constructions and noise threshold of topological subsystem codes. *Journal of Physics A: Mathematical and Theoretical*, 44(15):155301, 2011.
- [60] Brian Swingle. Rényi entropy, mutual information, and fluctuation properties of fermi liquids. *Physical Review B*, 86(4):045109, 2012.
- [61] Tiamhock Tay and Olexei I. Motrunich. Variational study of J_1 - J_2 heisenberg model on kagome lattice using projected schwinger-boson wave functions. *Phys. Rev. B*, 84:020404, Jul 2011.
- [62] Christophe Vuillot. Planar floquet codes. *arXiv preprint arXiv:2110.05348*, 2021.
- [63] Xiao-Gang Wen. *Quantum field theory of many-body systems: from the origin of sound to an origin of light and electrons*. OUP Oxford, 2004.
- [64] Simeng Yan, David A. Huse, and Steven R. White. Spin-liquid ground state of the $\sum_i |i_s\rangle |i_\ell\rangle = 1/2$ kagome heisenberg antiferromagnet. *Science*, 332(6034):1173–1176, 2011.
- [65] Hong Yao and Xiao-Liang Qi. Entanglement entropy and entanglement spectrum of the kitaev model. *Physical review letters*, 105(8):080501, 2010.
- [66] Beni Yoshida. Decoding the entanglement structure of monitored quantum circuits. *arXiv preprint arXiv:2109.08691*, 2021.
- [67] Aidan Zabalo, Michael J Gullans, Justin H Wilson, Sarang Gopalakrishnan, David A Huse, and JH Pixley. Critical properties of the measurement-induced transition in random quantum circuits. *Physical Review B*, 101(6):060301, 2020.
- [68] Paolo Zanardi, Daniel A Lidar, and Seth Lloyd. Quantum tensor product structures are observable induced. *Physical review letters*, 92(6):060402, 2004.
- [69] Zhenyue Zhu and Steven R. White. Spin liquid phase of the $s = \frac{1}{2}$ $J_1 - J_2$ heisenberg model on the triangular lattice. *Phys. Rev. B*, 92:041105, Jul 2015.

Appendix A: Entanglement entropy of the steady state

In this section, we will explain how to compute the entanglement entropy of a subset of spins using the Majorana fermion picture. In particular, we show that the entanglement entropy of a region A (with smooth boundaries) can be written as

$$S(A) = \frac{1}{2}n_p + \frac{1}{2}n_c - 1, \quad (\text{A1})$$

where n_p is the number of plaquettes on the boundary of A and n_c is the number of Majorana dimers with one end in A and the other in $B = \bar{A}$ before projecting back to the spin Hilbert space.

In general, for a stabilizer state of n qubits with the stabilizer group \mathcal{G} , let $\mathcal{G}_A \subseteq \mathcal{G}$ be the subgroup of stabilizers which act trivially on B . Define \mathcal{G}_B analogously. Then let the subgroup \mathcal{G}_{AB} to be the group that is generated by the remaining $n - \text{rank}(\mathcal{G}_A) - \text{rank}(\mathcal{G}_B)$ additional generators needed to generate \mathcal{G} , i.e.

$$\mathcal{G} = \mathcal{G}_A \cdot \mathcal{G}_B \cdot \mathcal{G}_{AB}. \quad (\text{A2})$$

With an abuse of notation, one may write \mathcal{G}_{AB} as the quotient group $\mathcal{G}/(\mathcal{G}_A \cdot \mathcal{G}_B)$. The entanglement entropy of the region A is given as [13],

$$S(A) = \frac{1}{2} \text{rank}(\mathcal{G}_{AB}). \quad (\text{A3})$$

The stabilizer group of the steady state is generated by the set of all plaquette operators and a set of string operators obtained via projecting Majorana dimers into the spin Hilbert space. Let $\tilde{\mathcal{G}}_{AB}$ be the group that is generated by the plaquette operators on the boundary of A and the string operators with one end point in A and the other in B . Clearly, $\mathcal{G}_{AB} \subseteq \tilde{\mathcal{G}}_{AB}$. However, in general it might be possible to combine some generators of $\tilde{\mathcal{G}}_{AB}$ with other generators \mathcal{G} such that the result is localized in either localized in A or in B . In the following we show that there are 2, and only 2 such relations.

Given that the product of a subset of plaquette operators corresponds to a set of closed loops on the lattice, it is clear that the only way such a product with some plaquettes on the boundary can be localized in A or B is to consider the product of all of plaquettes on the boundary. This results in two loops, one inside A and one inside B . Then one can shrink away the inside loop via multiplying it with plaquette operators inside A arriving at something with a support only in B .

Now let us consider a product which also includes a subset of the string operators from $\tilde{\mathcal{G}}$. Such an operator can be represented by a set of end points (which are fixed by the choice of the subset of string operators that appear in the product) and a set of strings that connect them. In what follows we show that to cancel the support of such a product in B , the product must include *all* the lattice points in B as end points. Imagine it has an end

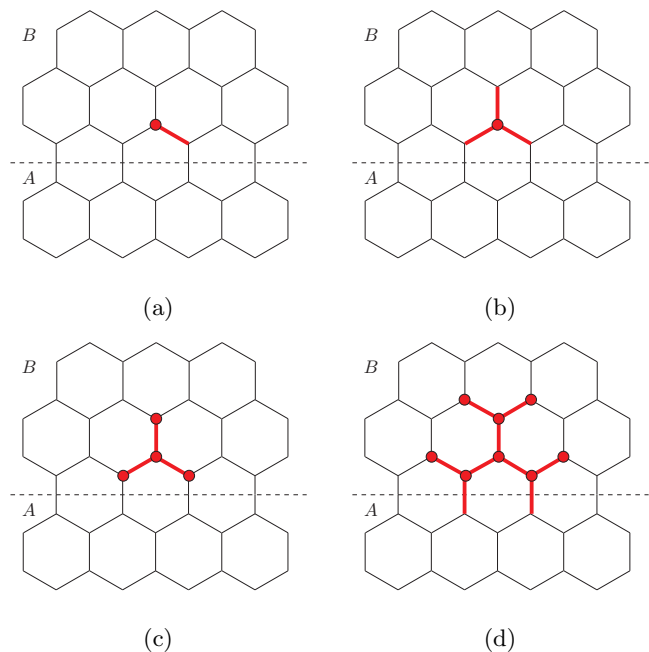


FIG. 22: If P is a non-trivial product of string operators and plaquette operators that acts trivially in region B , then it should include all points in region B as end points of string operators. Say P includes a string operator with the end point shown in panel (a). For P to act trivially on the red dot qubit, it should include another string operator which passes through the two remaining bonds as shown in panel (b). But to have trivial support on the neighboring sites as well, the neighboring sites should also be end points of string operators that are included in P , as shown in panel (c). By repeating the same argument for these new end points, one can see the neighboring sites shown with red dots in panel (d) should also be end-points of string operators included in P . This line of argument then shows that P should include all sites in region B as end point.

point denoted by the red dot in Fig. 22a as an endpoint of a string operator whose last segment is shown by a thick red line. Now, the only way for this operator to act trivially on the red dot qubit is if there is another string that passes through the other two bonds connected to the red dot vertex (Fig. 22b). But since the operator has to act trivially on the neighboring sites too, there has to be endpoints on neighboring sites as well (Fig. 22c). Now we can repeat the same argument for these new endpoints to show that there should be endpoints on all next neighboring sites in B as well (Fig. 22d) and so on. Indeed, such a product exists and it can be found with a procedure similar to what was outlined in Appendix G. The important point that the above argument shows is that it is the only non-trivial product with trivial support

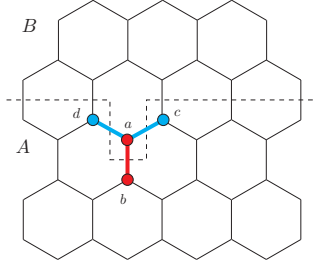


FIG. 23: One can cancel the support of $g_{a,b}$ (red) in B by multiplying it with $g_{d,e}$ (blue), resulting in an operator that is entirely supported on A .

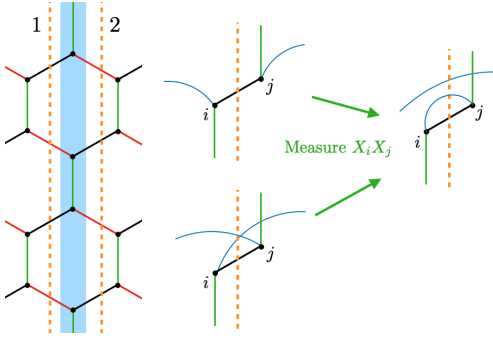


FIG. 24: Under projective measurements of the bond operators on bonds, the dynamical rules for the evolution of dimer configurations leads to the conservation of dimer number parity across vertical cuts, such as the one shown in (a).

on B . Therefore, we find that,

$$\text{rank}(\mathcal{G}_{AB}) = \text{rank}(\tilde{\mathcal{G}}_{AB}) - 2 = n_p + n_c - 2. \quad (\text{A4})$$

Plugging Eq.(A4) into Eq.(A3) then yields the desired result.

It is worth mentioning that if the boundary between A and B is not smooth, this argument could fail. A counter example is shown in Fig.23; $g_{a,b}$ has non-trivial support in both A and B . But, one could multiply it with just $g_{c,d}$ (which has both endpoints in A) to arrive at an operator with trivial support on B .

Appendix B: Dimer Number Parity

Consider the honeycomb lattice with periodic boundary conditions and so that each site is paired with another unique site. We consider a vertical “cut” through the x and y -type bonds of the honeycomb lattice, as shown by the dotted orange line labeled “1” in Fig. 24. We now show that the *number parity* of dimers crossing this cut – given by $(-1)^{n_1}$ where n_1 is the number of dimers which straddle the cut labeled “1” – is the same for all vertical cuts on the honeycomb lattice. The number of dimers

crossing a cut is a well-defined quantity if the dimers are short-ranged. An example of another such vertical cut, labeled “2”, is also shown in Fig. 24a. The proof of this statement is obtained as follows. First, consider the column of s sites which are shaded in blue in Fig. 24a; s is an even integer since each unit cell on the honeycomb lattice contains two lattice sites. Let $n_\ell(n_r)$ be the number of dimers which contain one endpoint in the shaded blue column and another endpoint to the left (right) of the column, respectively. The remaining $s - n_\ell - n_r$ sites in the shaded blue column are dimerized with each other, so that $s - n_\ell - n_r$ is an even integer. Since s and $s - n_\ell - n_r$ are both even, we must have that $n_\ell + n_r$ is even so that $(-1)^{n_\ell} = (-1)^{n_r}$. Let n_1 and n_2 be the total number of dimers straddling cut 1 or cut 2, respectively. These two quantities are related as

$$n_2 = n_1 - n_\ell + n_r \quad (\text{B1})$$

and as a result

$$(-1)^{n_1} = (-1)^{n_2}. \quad (\text{B2})$$

This completes the proof.

Finally, we observe that the dynamical rules for the evolving configuration preserve the parity along the vertical cut. This is trivially shown by considering the effect of a bond measurement on the dimers crossing a vertical cut passing through that bond. If the sites were already dimerized with each other, then the measurement has no effect on the state of the system. Now consider the case where the sites are dimerized with other sites in the system. The sites could be dimerized with two other sites on (i) opposite sides of the vertical cut or (ii) on the same side. The former case, and the dimer configuration after a bond measurement, are shown in Fig. 24b. The dimer number parity crossing the cut is manifestly preserved by the measurement. Case (ii) can be similarly considered, to show that the bond measurements preserve the dimer number parity across a vertical cut.

Appendix C: Mutual Information in Free Fermion systems

1. Free Fermions with a Fermi surface

a. 1d

Consider a 1d system of free fermions. Let the subsystem A be composed of disjoint intervals (u_1, v_1) , (u_2, v_2) , ..., (u_N, v_N) . The entanglement entropy of subsystem A

is [4]:

$$S_A = 1/3 \left[\sum_{k \leq j} \log((v_k - u_j)/a) - \sum_{k < j} \log((v_k - v_j)/a) - \sum_{k < j} \log((u_k - u_j)/a) \right]. \quad (\text{C1})$$

This expression shows that the mutual information is extensive in this system, in the sense that if A , B and C are three disjoint intervals, we have,

$$I(A : BC) = I(A : B) + I(A : C). \quad (\text{C2})$$

For two disjoint intervals of widths w_1 and w_2 , separated by distance d , the mutual information would be,

$$I(A : B) = \frac{1}{3} \log \left(\frac{(d + w_1)(d + w_2)}{d(d + w_1 + w_2)} \right), \quad (\text{C3})$$

which falls off as $w_1 w_2 / d^2$, for $d \gg w_1, w_2$.

In particular if we divide a circle of length L into four regions of equal size $L/4$ and A and B denote two antipodal regions, their mutual information would be,

$$I(A : B) = \frac{1}{3} \log 2. \quad (\text{C4})$$

We can also consider the tripartite mutual information between three adjacent intervals of length $L/4$. Eq.(C2) already suggests¹¹ that the tripartite mutual information would vanish in free fermions. We can use Eq. (C1) to explicitly compute the tripartite mutual information for three adjacent intervals of width w :

$$\begin{aligned} I(A : B : C) &= I(A : B) + I(A : C) - I(A : BC) \\ &= \frac{1}{3} \left[\log \left(\frac{w}{2a} \right) + \log \left(\frac{4}{3} \right) - \log \left(\frac{2w}{3a} \right) \right] \\ &= 0. \end{aligned} \quad (\text{C5})$$

b. $2d$

One may use the 1d result alongside the generalized Widom formula [60] to find the entanglement entropy of non-convex and/or disjoint regions in Fermi liquid systems in higher dimensions where the Fermi surface has co-dimension one:

$$S(R) = \frac{1}{(2\pi)^{d-1}} \int dA_x dA_k |n_x \cdot n_k| \frac{S_{1+1}(x, k)}{n_{\text{int}}(x, k)}, \quad (\text{C6})$$

¹¹ Note that Eq.(C2) is only valid when the intervals are completely disjoint.

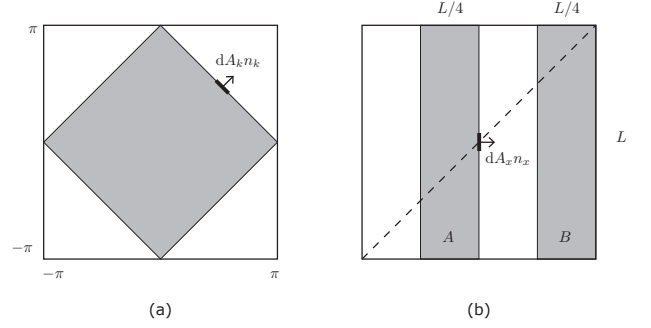


FIG. 25: (a) The Brillouin zone and the Fermi surface at half-filling. (b) Two cylinders (A and B) of width $L/4$ which are $L/4$ apart.

where dA_x and dA_k are area elements on the surface of the region R and the Fermi surface respectively, n_x and n_k are the unit normals at the respective points on those surfaces, $S_{1+1}(x, k)$ is the entanglement entropy of a 1d chiral mode on the subregion $R \cap L$, where L is the straight line passing through x in the direction of the Fermi velocity $v(k)$ and n_{int} is the number of times this line intersects with region R . Consider a tight binding free fermion system on a $L \times L$ periodic lattice at half-filling, where the fermi surface has the simple shape of a rotated square. By using the Widom formula, we find that the mutual information between two cylinders of length $L/4$ which are $L/4$ apart is (Fig. 25),

$$\begin{aligned} I(A : B) &= \frac{1}{2\pi} 4\sqrt{2}\pi \times 4L \times \frac{\sqrt{2}}{2} \times \frac{1}{4} \times \frac{1}{2} \times \frac{\log 2}{3} \\ &= \frac{\log 2}{3} L \end{aligned} \quad (\text{C7})$$

where the last $\frac{1}{2}$ factor is there since each chiral mode contributes half of the entanglement in Eq. (C1). As can be seen from the plot in Fig. 26a, this expression agrees perfectly with the numerical result. Moreover, by using Widom formula and Eq. (C5), one can see that the tripartite mutual information between the two cylinders and the one in between vanishes (see Fig. 26b).

2. Kitaev Honeycomb model

The Kitaev honeycomb model has two phases, gapped and gapless. Both phases are area law entangled. This means that the entanglement entropy of a $x \times L$ cylindrical region on a $L \times L$ torus is proportional to L . In the gapless phase, the subleading correction to the area law is a function of $u = x/L$ and it is proportional to $1/u$ for $u \ll 1/2$ and $1/(1-u)$ when $1-u \ll 1/2$ similar to the case for free 2d Dirac fermion [8]. The subleading terms in the gapped phase vanish much faster (probably exponentially in the correlation length) as expected (see Fig. 27). The leading term of the mutual information for

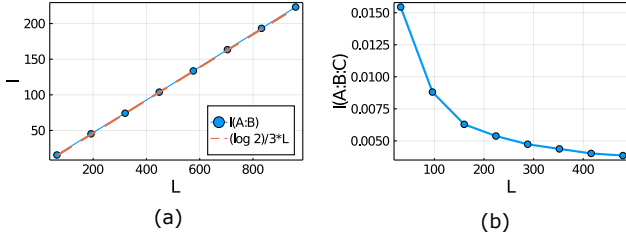


FIG. 26: (a) Mutual information of two cylindrical regions of width $L/4$ which are $L/4$ apart in half-filled free fermion on a periodic 2d square lattice. (b) The tripartite mutual information between the aforementioned cylinders and the one in between. Instead of considering half filled system, we set $\mu = -0.3$ to avoid numerical instabilities.

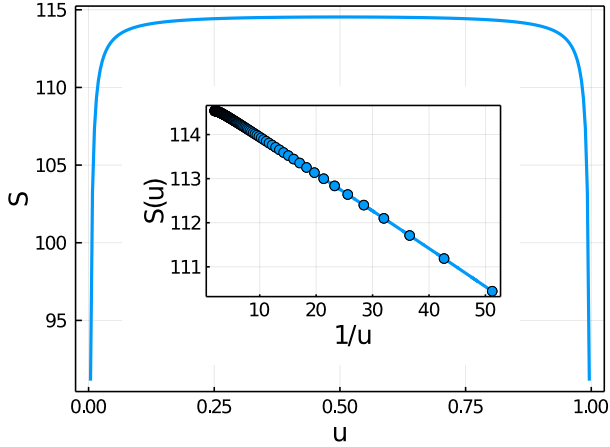


FIG. 27: Entanglement entropy of a $x \times L$ cylindrical region of the Kitaev honeycomb model on a $L \times L$ torus as a function of $u = x/L$ at the isotropic point $J_x = J_y = J_z$ for $L = 256$.

Dirac fermions is computed in Ref. [7]; for two circular regions of radius R and R' which are distance r apart, the mutual information would be only a function of the cross ratio

$$z = \frac{4RR'}{r^2 - (R - R')^2}, \quad (\text{C8})$$

and scales as

$$I(z) = \frac{1}{15}z^2 + \dots \quad (\text{C9})$$

for $z \ll 1$. The mutual information being only a function of dimension less z means it remains constant when R , R' and r are all scaling proportionally, which is similar to the case we are studying on a toroidal geometry. Fig. 28 shows the mutual information between two cylinders of size $L/4 \times L$ which are distance $L/4$ apart, for the Kitaev model in the gapless phase, on the phase boundary and in

the gapped phase. As we expect from the Dirac fermion, the mutual information saturates to a constant value in the gapless phase. Interestingly, at the phase boundary the mutual information seems to grow as \sqrt{L} . In the gapped phase it goes to zero, as expected from a finite correlation length.

The tripartite mutual information between three adjacent cylinders also vanishes similar to the free fermion case (see Fig. 29).

Appendix D: Percolation phase transitions at the boundary of the phase diagram

Here, we will show that the entanglement dynamics at the boundary of the phase diagram maps to L decoupled classical 2D bond-percolation problems.

For concreteness let us focus on the $p_y = 0$ boundary. We partition the lattice into L rows, where each row is comprised of x and z bonds. When $p_y = 0$, no inter-row operator is going to be measured, hence the entanglement dynamic of each row is completely decoupled from the others.

In the following we consider the entanglement dynamics of a single row. We label the spins by an index $j = 1, \dots, 2L$. The circuit is then comprised of random measurements of the following operators,

$$A_i = X_{2i-1}X_{2i}, \quad (\text{D1})$$

$$B_i = Z_{2i}Z_{2i+1}, \quad (\text{D2})$$

for $i = 1, \dots, L$. On the other hand the following set of operators commute with all A_i and B_i operators

$$S_i = X_{2i}X_{2i+1}, \quad \text{for } i = 1, \dots, L, \quad (\text{D3})$$

and as such we may regard them as symmetries of the circuit. For simplicity, let us assume that the initial state is in the symmetry sector with $S_i = +1$ for all i , e.g. $|+\rangle^{\otimes 2L}$. Finally, we map this circuit to the $XX - Z$ measurement-only random circuit which has been studied thoroughly before[22, 32, 33, 53]. In particular, it has been shown that the entanglement dynamics is described by the 2d classical bond-percolation problem. To this end, we consider the dual circuit under the local unitary

$$U = \bigotimes_i \text{CNOT}_{2i,2i+1} \quad (\text{D4})$$

where $\text{CNOT}_{i,j}$ is the CNOT gate with qubit i as the control and qubit j as the target. Under this unitary, A_i , B_i and S_i transform as,

$$A_i \mapsto X_{2i-1}X_{2i}X_{2i+1}, \quad (\text{D5})$$

$$B_i \mapsto Z_{2i+1} \quad (\text{D6})$$

$$S_i \mapsto X_{2i}. \quad (\text{D7})$$

Since we have assumed the initial state is in the symmetry sector $S_i = +1$, the local unitary disentangles the spins with even index into the $X_{2i} = +1$ state. Therefore, in the dual picture, the circuit is basically consisted of the random measurement of Z_{2i+1} and $X_{2i-1}X_{2i+1}$.

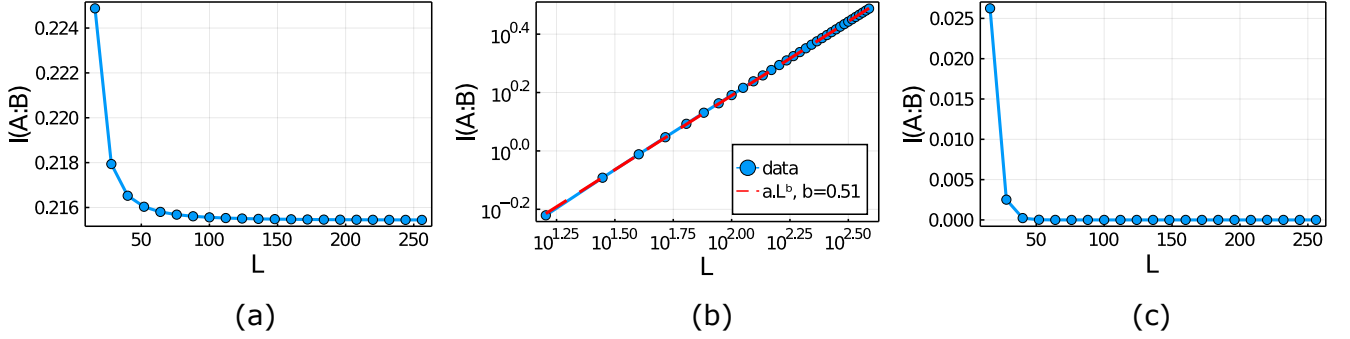


FIG. 28: Mutual information in of two antipodal cylinders of length $L/4$ in the ground state of Kitaev at $J_y = J_z = 1$ and (a) $J_x = 1$, (b) $J_x = 2$ and (c) $J_x = 3$.

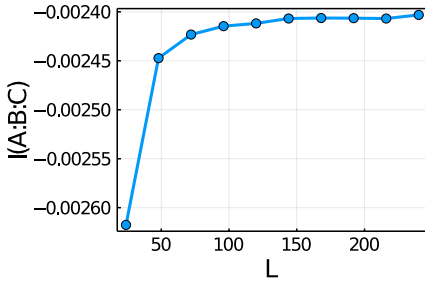


FIG. 29: Tripartite mutual Information between three cylinders of length $L/4$ for the Kitaev honeycomb model on a $L \times L$ torus.

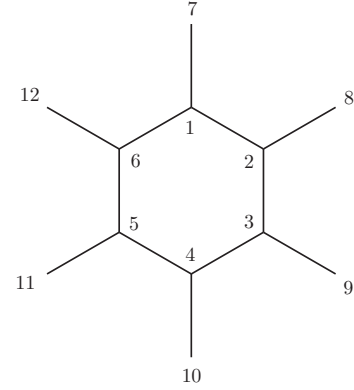


FIG. 30: the qubits on a plaquette of the Honeycomb lattice as well as the neighboring qubits.

Appendix E: Plaquette operators measurement rate

We show that there is a constant $c > 0$ such that the probability of a given plaquette being measured during 6 consecutive time steps is lower bounded by c . Let q denote such a probability.

For simplicity, we consider the isotropic point $p_x = p_y = p_z$, but it is clear that the same statement holds as long $p_x, p_y, p_z > 0$. Consider a plaquette shown in Fig.30, where numbers represent the qubits on the corresponding sites. Let E_{ij} denote the link operator associated to the edge between qubits i and j . Consider the collection of twelve link operators $C = \{E_{ij}\}$ shown in Fig.30. At each time step, N link operator gets measured randomly. The probability that at least one link from C gets measured in a time step is given by $1 - (1 - \frac{12}{3N/2})^N \simeq 1 - e^{-8}$, where N is the total number of qubits¹². Let P_6 be the probability that during 6 consecutive time steps, at least 6 times a link from C gets measured. Of course, it needs not to be the same link all the 6 times. P_6 can be lower

bounded easily as,

$$P_6 \geq (1 - e^{-8})^6 \simeq 1 - 6e^{-8}. \quad (\text{E1})$$

Considering the 6 consecutive times that links from C have been measured, there is a probability of $(1/12)^6$ that it is the following sequence of link operators that has been measured:

$$E_{1,2}, E_{3,4}, E_{5,6}, E_{2,3}, E_{4,5}, E_{6,1}, \quad (\text{E2})$$

in which case the corresponding plaquette operator would have been measured. Note that this is true independent of the way the links not shown in Fig.30 gets measured. Therefore the probability of a plaquette being measured during 6 consecutive time steps is lower bounded by

$$q \geq P_6 \times (1/12)^6 \geq (1 - 6e^{-8})/12^6 > 0. \quad (\text{E3})$$

Since this lower bound is positive and independent of the system size, it shows that each plaquette are being measured at least with constant rate, independent

¹² Note that there are $3N/2$ edges in a Honeycomb lattice with N vertices.

of the system size. Therefore, it only takes $O(\log L)$ time steps for all plaquettes to be measured. We note that the actual rate at which plaquettes are being measured could be much larger than the analytical lower bound in Eq.(E3)(See Fig.39b in Appendix I).

Appendix F: Purification in the Critical Phase

Starting from a maximally-mixed initial state, we argue that in the critical phase, the system disentangles as a power law $S(t) \sim t^{-1}$ in time as projective measurements are performed. Within a short time $t_* \sim O(\log L)$ after starting to perform measurements of the bond operators, the plaquette stabilizers W_p become part of the stabilizer group. To study the subsequent purification dynamics of the system, it is convenient to consider the following density matrix for the Majorana partons

$$\rho_f \sim |\Psi_b\rangle \langle \Psi_b| \otimes \mathbf{1} \quad (\text{F1})$$

where $|\Psi_b\rangle$ is a pure state of the b Majorana fermions, as described below Eq. (2) in which each b Majorana fermion is dimerized with its nearest-neighbor $(ib_{\mathbf{r}}^j b_{\mathbf{r}'}^j |\Psi_b\rangle = |\Psi_b\rangle$ where \mathbf{r} and \mathbf{r}' are sites at the ends of a bond of type j). The c Majorana partons are in a maximally-mixed initial state. The density matrix of the spin degrees of freedom

$$\rho \propto \prod_p \frac{1 + W_p}{2} \quad (\text{F2})$$

clearly describes a volume-law-entangled state.

As measurements of the bond operators are performed, the measured bonds become part of the stabilizer group that describes the evolving, monitored state. Consider measuring $X_{\mathbf{r}} X_{\mathbf{r}'}$ (where \mathbf{r} and \mathbf{r}' are sites connected by an x -type bond). Since $X_{\mathbf{r}} X_{\mathbf{r}'} = c_{\mathbf{r}} b_{\mathbf{r}}^x b_{\mathbf{r}'}^x c_{\mathbf{r}'}$, a measurement of this operator in the state (F2) is equivalent to adding $\pm i c_{\mathbf{r}} c_{\mathbf{r}'}$ as a stabilizer to the evolving state of the Majorana partons. We refer to $c_{\mathbf{r}}$ and $c_{\mathbf{r}'}$ as “paired” Majorana partons since they are dimerized and belong to the stabilizer group for the density matrix of the fermions after measuring $X_{\mathbf{r}} X_{\mathbf{r}'}$.

The “unpaired” c Majorana partons each provide an $O(1)$ contribution to the entanglement entropy of the entire system. To understand the purification of the evolving state, we investigate how these unpaired degrees of freedom are “annihilated” (become paired) as measurements are performed. First, we note that the unpaired Majorana partons can only annihilate when two of them become nearest-neighbors, and the corresponding bond operator connecting the two is measured. It is easily checked that a measurement of a bond operator connecting two Majorana partons in which at least one is unpaired, will not change the number of independent generators of the stabilizer group for ρ_f . Consider, for example, a measurement of $X_{\mathbf{r}} X_{\mathbf{r}'} = c_{\mathbf{r}} b_{\mathbf{r}}^x b_{\mathbf{r}'}^x c_{\mathbf{r}'}$ in a state

ρ_f where $i c_{\mathbf{r}} c_{\mathbf{s}} = +1$ where \mathbf{s} is another site in the system, and where $c_{\mathbf{r}'}$ is unpaired. After this measurement, $\pm i c_{\mathbf{r}} c_{\mathbf{r}'}$ belongs to the stabilizer group, while $c_{\mathbf{s}}$ is now unpaired. As a result, the measurement has the effect of moving the unpaired Majorana parton from \mathbf{r} to \mathbf{s} .

In the critical phase, the probability distribution of string stabilizer lengths (the Cartesian distance between their endpoints) decays as a power-law, as reviewed in Sec. II A; equivalently, in the parton description of the steady-state, the probability that a Majorana $c_{\mathbf{r}}$ is paired with another Majorana $c_{\mathbf{r}+\mathbf{s}}$ at relative separation \mathbf{s} decays as $P(\mathbf{s}) \sim |\mathbf{s}|^{-3}$. To understand the purification dynamics in the critical phase, we now assume a dilute concentration of the unpaired c Majoranas, and that the probability that a given *paired* Majorana is dimerized with another Majorana fermion at relative separation \mathbf{r} is again given by $P(\mathbf{r})$. As bond measurements are performed, the dynamics of an unpaired Majorana degree of freedom is then described by a random walk, where probability density per unit time for a step in the direction \mathbf{r} is given by $P(\mathbf{r})$. The variance in the distribution of step lengths $\langle |\mathbf{r}|^2 \rangle = \int |\mathbf{r}|^2 P(\mathbf{r}) d^2 \mathbf{r}$ is infinite, so that the wandering of a given unpaired Majorana is dominated by rare “long” steps; such a random walk is known as a Lévy flight¹³.

The unpaired Majorana degrees of freedom wander and “annihilate” by pairing with other unpaired Majoranas. To understand how they wander and annihilate, we define a coarse-grained density $n(\mathbf{r}, t)$ of the unpaired degrees of freedom and compare two ways in which these Majorana degrees of freedom may annihilate: (i) Unpaired Majorana degrees of freedom may annihilate when they are sufficiently close together; in this case, the rate $\Gamma(n)$ at which the Majorana degrees of freedom annihilate is proportional to the local density $\Gamma(n) \propto n$; (ii) Unpaired Majorana degrees of freedom annihilate by taking rare “long” steps. Let $P(\mathbf{r}) \sim |\mathbf{r}|^{-\Delta}$ ($\Delta = 3$ in our case of interest). In a time t an unpaired Majorana degree of freedom will travel a distance $O(t^{1/(\Delta-2)})$; this can be argued by observing that the evolution of the local density in the absence of annihilation events is given by

$$\frac{\partial n(\mathbf{r}, t)}{\partial t} = \lambda \int d^2 \mathbf{r}' P(\mathbf{r}') [n(\mathbf{r} - \mathbf{r}', t) - n(\mathbf{r}, t)] \quad (\text{F3})$$

The evident re-scaling of space and time that leaves (F3) invariant leads to the typical distance travelled by an unpaired degree of freedom in a time t . In two spatial dimensions, the typical spacing between unpaired Majoranas in a region with density $n(\mathbf{r}, t)$ is $n(\mathbf{r}, t)^{-1/2}$. As a result, the annihilation rate due to long steps in a Lévy flight, obtained by estimating the typical time to traverse this distance, is $\Gamma(n) \sim n^{(\Delta-2)/2}$.

¹³ Random walks in d spatial dimensions where a displacement \mathbf{r} occurs with probability $P(\mathbf{r}) \sim |\mathbf{r}|^{-d-\sigma}$ and with $\sigma < 2$ define Lévy flights, for which $\langle |\mathbf{r}|^2 \rangle$ is divergent; see e.g. Ref. [42]

At long times, these respective processes lead to a decay of the density as $n \sim t^{-1}$ for process (i) and $n \sim t^{(2-\Delta)/2}$ for process (ii). As a result, when $\Delta < 4$ (for our case of interest, $\Delta = 3$), the the effective annihilation dynamics for the unpaired degrees of freedom leads to the long-time behavior $n \sim t^{-1}$. We conclude that the entanglement entropy of the system should decay as $S(t) \sim t^{-1}$ in the critical phase.¹⁴

Appendix G: Mutual information in the area law phase

Here we explain why $I_2(A : C) = 1$ throughout the area law phase. The $p_y = p_x \rightarrow 0$ limit has been explained in Section IV C. Here we consider the case when p_x and p_y are finite.

Let $g_{a,b}$ denote the string operator which connects a to b . It has been already noted that the specific path which connects a to b does not matter in the sense that any two paths give rise to the same string operator up to a product of plaquette operators. Now consider the product of two string operators $g_{a,b} g_{c,d}$. Interestingly, this operators can also be specified only by its end points a,b,c and d . i.e. not only the paths connecting the endpoints do not matter, but all different pairing of the endpoints are equivalent up to product of plaquette operators. e.g.

$$g_{a,b} g_{c,d} = g_{a,d} g_{c,b} S \quad (\text{G1})$$

where S is a product of plaquette operators (On a torus, S could include the long cycle stabilizers as well). This is due to the simple fact that $g_{a,b} g_{c,d} \times g_{a,d} g_{c,b}$ is a string operator without a boundary. More generally, $g_{a,b} g_{c,d} \cdots g_{e,f}$ is equivalent to $g_{\pi(a),\pi(b)} g_{\pi(c),\pi(d)} \cdots g_{\pi(e),\pi(f)}$ where π is an arbitrary permutation on the set of end points. This means a product of string operators can be specified by its set of endpoints and the specific pairing of the endpoints does not matter.

Now consider a typical state in the area law phase. Let P be the product of all string operators which have at least one end point in the region B . As we discussed above P can be specified by a set of end points. This set of end points include all points inside B plus some points in A and C near the boundaries of B (Fig.31a). Now choose a specific pairing of the end points, where all points in the bulk of B are paired along the z bonds, and the end points next to the boundary are paired with the endpoints which are in A or C , and any remaining endpoints on each side (near AB boundary and near AC boundary) will be paired together(Fig.31b). This pairing

will be possible as long as the parity of the number of endpoints in A is the same as the parity of number of z bonds that crosses the A and B boundary (Note that the parity of number of endpoints in A and C are the same). For now we assume this is the case and we will provide an argument in its support later. Let P' denote the operator corresponding to this specific pairing. Now consider the operator C which is the product of P' with all plaquette operators on every other row of B (shown as yellow in Fig.31c). Note that C has non-trivial support only on A and C and it acts trivially in B , hence it could contribute to $I_2(A : C)$.

To see that the parity of end points in A are the same as the parity of the number z bonds between A and B , note that we expect the state to be close to the state where all dimers are along the z bonds (as in Fig.12), in the sense that if one uses the latter state as the initial state of the circuit, it will evolve into the former state with only local rearrangement of the dimers without generating long range strings. In this case, we can use the fact that the parity of dimers crossing a line is an invariant of the circuit dynamics to reach the desired result.

Appendix H: Stability of phases under single qubit measurements.

In Section V we argued that measuring plaquette operators directly with a rate $p_{\text{plq}} \gg p_s$ would stabilize both phases against single qubit measurements. Given that in the original circuit model plaquette operators are also measured with constant rate, it follows that both phases are robust against small rates of single qubit measurements. The only caveat is that in the original model, plaquette operators are not measured directly, but rather through a sequence of bond measurements, which in turn might cause proliferation of defects introduced via Z measurements. In this section, we show that this will not happen, i.e. measuring plaquette operators directly or through a series of bond measurements will likely have the same effect.

In the absence of perturbation, the steady state stabilizer group is generated by two types of stabilizers: 1) the plaquette stabilizers and 2) the string operators. Without perturbations, the plaquette operators do not have any dynamics while the string operators follow a dynamic similar to the parton dynamics described in Section II A: when a bond operator is measured, the two string operators with endpoints on that bond will be replaced by a string operator that is obtained from connecting the two, and the bond operator itself.

After a single qubit measurement, the two adjacent plaquette operators will be replaced in the generating set by their product and a single qubit Z operator. We denote the latter by g_z . The new stabilizer group has three types of generators: 1) plaquette operators, 2) string operators (which have remained unchanged) and 3) one g_z stabilizer. The important observation to make is that,

¹⁴ A simple generalization of this argument for a distribution $P(\mathbf{r}) \sim |\mathbf{r}|^{-d-\sigma}$ in d spatial dimensions can be used to show that process (i) dominates over (ii) at long times whenever $d > \sigma$ when $\sigma < 2$.

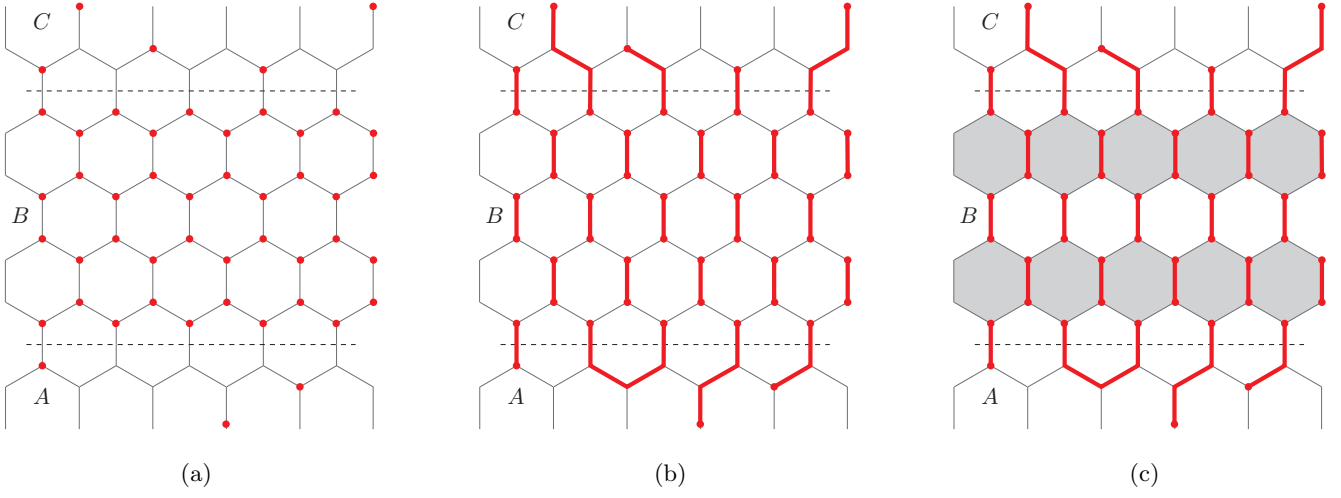


FIG. 31: Evaluating $I(A : C)$ in the area law phase: Let P be the product of all string operators which has at least one end point in region B . A typical set of end points specifying P is shown in panel (a). Up to multiplication by plaquette operators, P can be taken to be the product of the string operators shown in panel (b). The product of the shaded plaquette operators and the red string operators in panel (c) has non-trivial support only in A and C and thus contributes to $I(A : C)$.

the presence of g_z in the generating set has no effect on the dynamics of the string and plaquette operators under the subsequent bond measurements (although g_z has its own dynamic). As such, after a constant time, the

removed stabilizers will be added to the generating set again, at which point g_z will be removed since the set of independent generators can not have more than $N = L^2$ elements.

Appendix I: Supplementary Figures

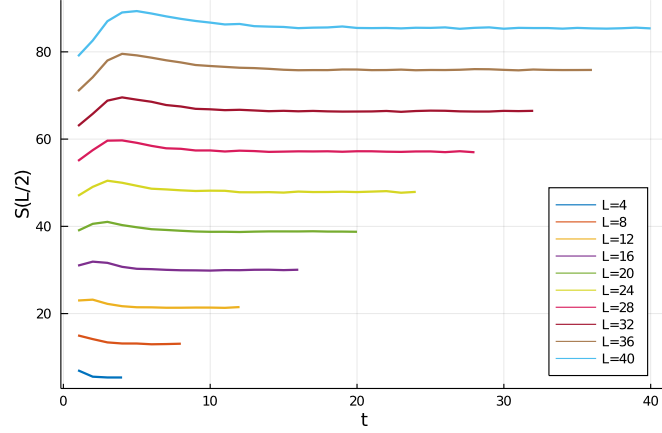


FIG. 32: Entanglement entropy of a cylinder of size $L/2 \times L$ as a function of time at the isotropic point $p_x = p_y = p_z$, starting from a state which is a projection onto the subspace where all stabilizers (plaquettes + long cycles) and all the z -bond operators have some definite value, say $+1$. It is clear from the plot that the entanglement entropy is saturated at the final value after time $t = L$. This should be contrasted to the case when one starts from a totally mixed initial state, where one needs to wait for $t = O(L^2)$ time steps for the system to reach the steady state.

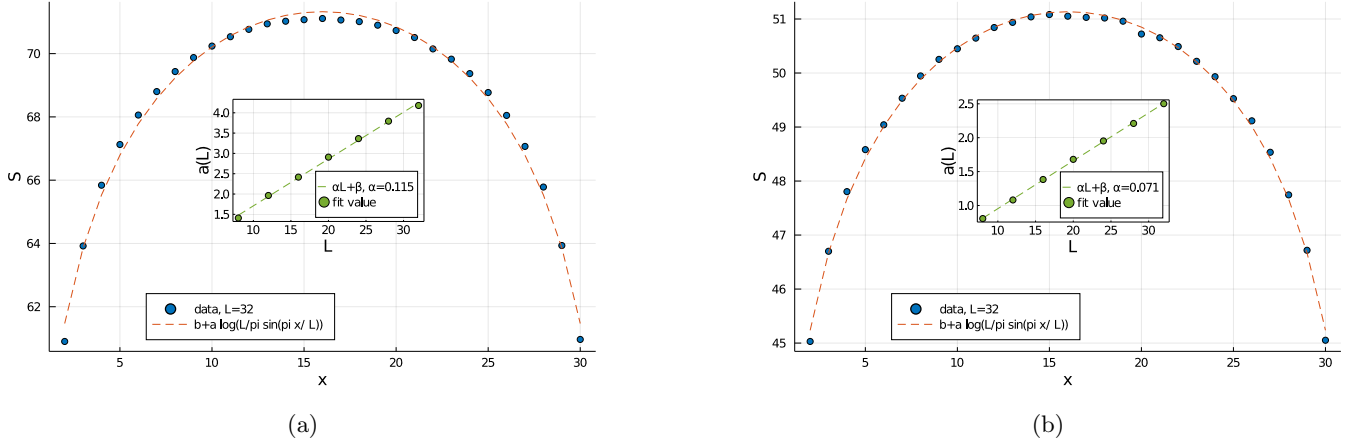


FIG. 33: Entanglement entropy of cylindrical region of size $x \times L$ for the steady state of the circuit model at $p_x = p_y = 0.2$ in the critical phase when (a) the boundary cuts through the Z -bonds and (b) when the boundary cuts through the X -bonds. Note that the best fit value of a is different for different cuts, and they are different from their value at the isotropic point $p_x = p_y = p_z$ (see Fig.10)

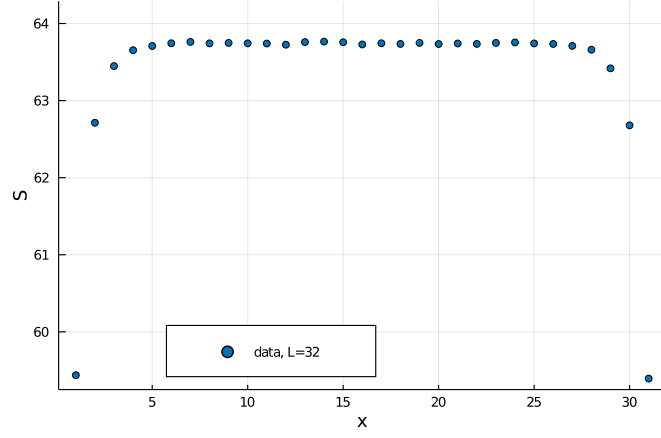


FIG. 34: Entanglement entropy of cylindrical region of size $x \times L$ for the steady state of the circuit model at $p_x = p_y = 0.1$, which clearly indicates an area law scaling of entanglement.

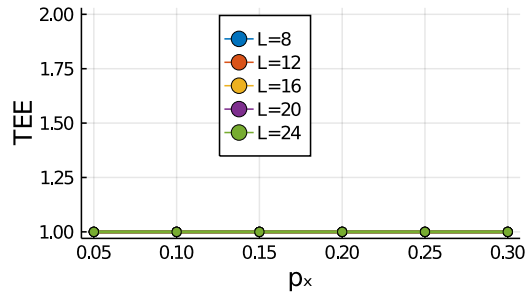


FIG. 35: Topological entanglement entropy in the steady state versus p_x on the symmetric line $p_x = p_y$. As is clear from the figure the topological entanglement entropy is always 1 irrespective of whether the system is in the area law phase or the critical phase. This is due to the fact that the plaquette operators belong to the stabilizer group of the steady state in both phases.

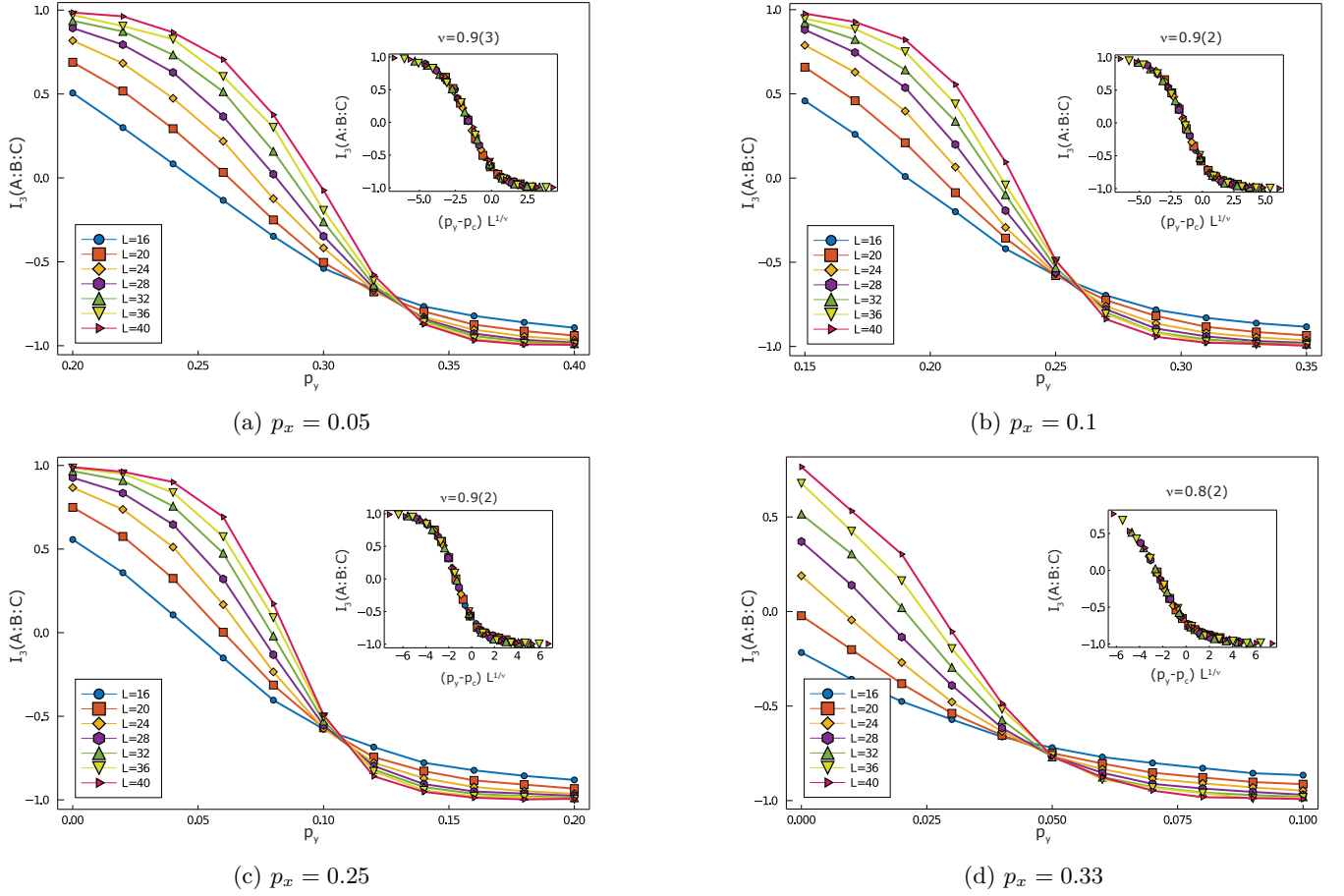


FIG. 36: The tripartite mutual information $I_3(A : B : C)$ versus p_y for fixed (a) $p_x = 0.05$, (b) $p_x = 0.1$, (c) $p_x = 0.25$ and (d) $p_x = 0.33$. The regions A , B and C are chosen according to Fig.11. The inset in each plot shows the corresponding data collapse. The estimate for the correlation length critical exponent which is found via data collapse is shown above each inset plot. Note that the critical points of subplots (a) and (d) as well as the critical points of subplots (b) and (c) are related by a reflection along z bonds.

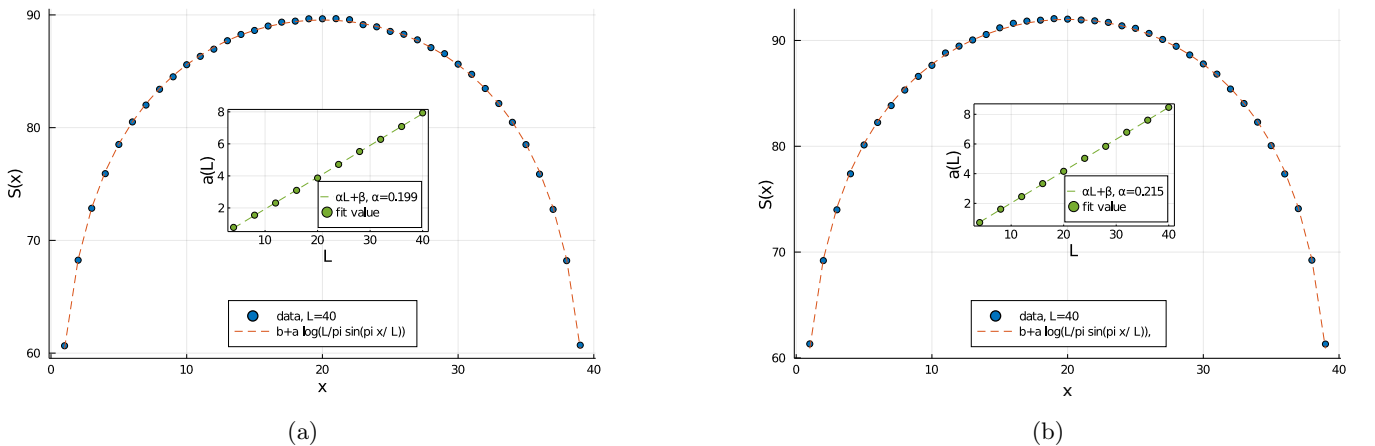


FIG. 37: The entanglement entropy of a cylinder of size $x \times L$ in the steady state of the monitored circuit where at each step either a product of two adjacent bond operators is measured randomly with probability p_3 or a random bond operator is measured randomly with probability $1 - p_3$. (a) corresponds to $p_3 = 0.05$ and (b) corresponds to $p_3 = 0.1$. The inset shows the best fit value of a versus system size L which shows a clear linear scaling, indicating a $L \log L$ violation of the area law.

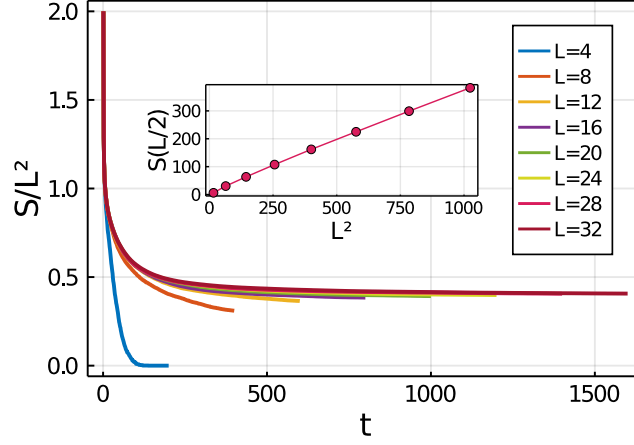


FIG. 38: The entanglement entropy of the system at the isotropic point $p_x = p_y = p_z$ subjected to random single qubit Z measurements with probability $p_s = 0.01$, starting from a totally mixed initial state. As can be seen from the figure, the entropy plateaus at a value proportional to L^2 which means that the steady state has volume law entanglement entropy. The inset shows the entanglement entropy of a half torus cylinder of size $L \times L/2$ in the pure steady state versus L^2 which scales linearly.

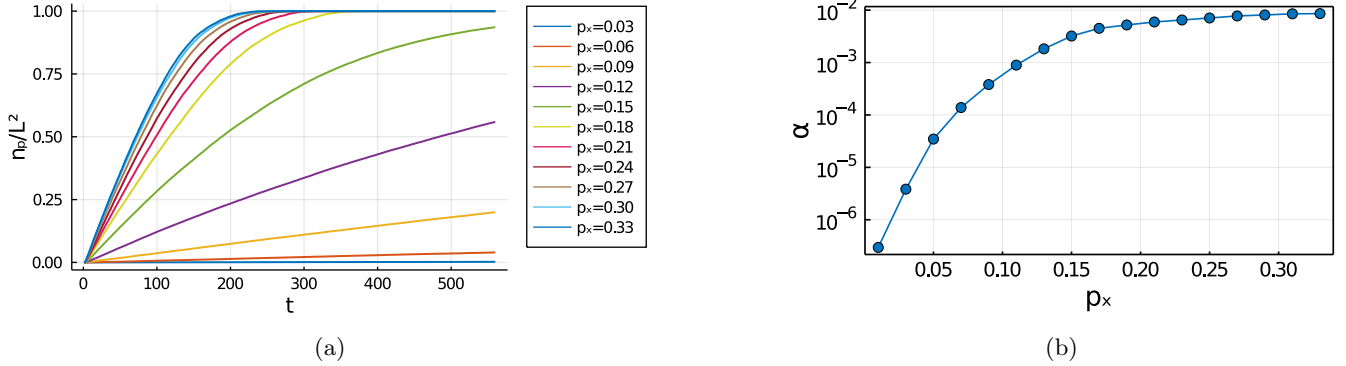


FIG. 39: (a) The fraction of plaquette operators that are in the stabilizer group as a function of time (b) The rate α of measuring a plaquette operator versus p_x along the symmetric line $p_x = p_y$. For each p_x , α is found by fitting the analytic form $n_p/L^2(t) = 1 - \exp(-\alpha t)$ to the data shown in the left panel, for $t = 10 - 20$.